Eleventh International Conference on Computational Fluid Dynamics (ICCFD11), Maui, HI, July 11-15, 2022

ICCFD11-2022-0903

Validation of Actuator Disk, Actuator Line and Sliding Mesh Methods within the LAVA solver

Gerrit-Daniel Stich[*], Luis S. Fernandes[†], Jared C. Duensing[‡], Jeffrey A. Housman [§], Gaetan K. Kenway[¶], and Cetin C. Kiris [‖]

NASA Ames Research Center, M/S 258-2, Moffet Field, CA 94035

Abstract

In this study the implementation of actuator-disk, actuator-line and sliding-mesh methodologies in the Launch Ascent and Vehicle Aerodynamics (LAVA) solver is described and validated against several test-cases. The different models are validated against available numerical as well as experimental data. Both steady and unsteady Reynolds-Averaged Navier-Stokes (RANS) simulations using the Spallart Allmaras (SA) turbulence model are performed for several different configurations representative of aeroscience applications. The first part of the paper is focused on the verification and validation of the implemented propulsor models. The first validation case is a theoretical rotor in hover, compared with the 1D analytical solution derived from momentum theory. The second validation is the Rotor-Airframe Interaction Model of Georgia Institute of Technology (GIT), representing the application of actuator disks to top-mounted rotorcraft vehicles or unmanned aerial vehicles (UAVs). The third case is a representative configuration for tip-mounted rotor-craft vehicles such as NASA's X57 airplane. The second part of the paper shows the implemented models applied to realistic engineering configurations such as NASA's X57 airplane and the R4 Advanced Ducted Propellor (ADT). A modification to the actuator line method in order to represent the blade geometry more closely is proposed and comparisons with simulations modeling the blade utilizing a sliding-mesh approach are made.

1 Introduction

Several propulsion modeling capabilities have recently been implemented within the Launch Ascent and Vehicle Aerodynamics (LAVA) computational solver framework [1]. These propulsion models include an actuator-disk model, an actuator-line model, and the implementation of relative motion capabilities using a sliding mesh method. This study serves as a validation report for the propulsion models in the LAVA framework, and demonstrates the capabilities using test cases representative of a majority of aircraft propulsion applications. Three different application types have been identified. The first application being a tip-mounted open rotor, such as NASA's X57 Maxwell electric aircraft [2]. The second application is a top-mounted configuration, typically seen in helicopters or unmanned aerial vehicles (UAV). A bridge between tip- and top-mounted applications can often be found in so called electric vertical take-off and landing vehicles (eVTOL). Such vehicles often transition from a top-mounted rotor during take-off and landing to a tip-mounted rotor in forward flight. EVTOL have been gaining more traction in recent years and are likely to play a major role in the future [3]. An example of such a vehicle currently developed Joby Aviation's S2 and S4 air taxi 2.0 [4, 5]. The challenge of these kind of rotor simulations is in the interaction of the wake created by the propeller with downstream (and upstream) components of the aircraft like wings. This

[*]Science and Technology Corporation, gerrit-daniel.stich@nasa.gov
[†]Science and Technology Corporation, luismiguel.dossantosfernandes@nasa.gov
[‡]Computational Aerosciences Branch, jared.c.duensing@nasa.gov
[§]Computational Aerosciences Branch, jeffrey.a.housman@nasa.gov
[¶]Science and Technology Corporation, gaetan.k.kenway@nasa.gov
[‖]Computational Aerosciences Branch, cetin.c.kiris@nasa.gov

is specifically important as the induced swirl from the propeller significantly changes the aerodynamic performance of the aircraft. The third application is representative for internal turbo-machinery configurations commonly found in turbofans used in conventional commercial aircraft. While potential-flow-based methods have been used extensively in the past to investigate such propeller wake-wing interactions [6, 7, 8], they are ultimately limited by their simplification of the aerodynamics. However, they are very efficient and show good agreement with simple configurations. Higher fidelity methods like Euler or Reynolds-Averages Navier-Stokes (RANS) computational fluid dynamics (CFD) simulations have the potential of resolving most of the important features while still being computationally feasible. This can be as simple as an Euler simulation using an actuator disk method like the one presented in Loetstedt [9], which showed promising results, but deviated from experiments in the rotor wake. Higher fidelity methods like the one presented by Thom [10], which include the blade in the RANS simulation by the use of arbitrary motion with a sliding mesh interface, seem to significantly improve the accuracy of the prediction. However, the need for higher mesh resolution and overhead from the motion of the blade result in a more computationally expensive simulation. A compromise between the sliding mesh and actuator disk method might be the use of an actuator line method in which the rotor is represented by a temporarily varying body force that imposes a thrust and swirl on the flow through time-varying momentum and energy source terms. Such an example is given in Churchfield *et al.* [11] for a wind turbine application, though it can also be utilized for rotorcraft applications.

The paper is structured as follows. First, in Section 2 the implementations of the actuator disk, actuator line as well as sliding mesh methods are described. This is followed by part one of this study which aims at validation and verification of the implemented propulsion models on canonical test cases described in Section 3. In a first step the implementation of a source based actuator disk model is compared with an analytical solution derived from momentum theory for a rotor with constant load distribution in free-stream. The second case is representative for top-mounted rotors in forward flight and the interaction with a fuselage. This is done on a common test case introduced by Georgia Institute of Technology (GIT) and known as the GIT rotor-craft test-case [12]. Third, simulations for a rotor mounted at the tip of a simplified fuselage are performed with steady-state RANS. Different blade loading profiles have been applied and are compared to experiments from Samuelsson [13] as well as results from RANS simulations by Guzel [14]. Finally, in the second part of this paper we demonstrate how these implemented propulsion methods with increasing fidelity have been applied to NASA's Aeronautics Mission Research Directorate (ARMD) projects. The first application is NASA's X-57 Maxwell aircraft which is described in Section 4. For this realistic engineering study, the LAVA team has been collaborating with researchers from NASA Langley as well as NASA Armstrong Research Centers to generate and extensive aerodynamic database that contains aerodynamic coefficients. Ultimately, CFD predictions would serve to construct lower order aerodynamic models for system level analysis, as well as develop a flight simulator used to train pilots to handle a variety of nominal and off-nominal conditions. For the second application described in Section 5 simulations were performed for NASA's R4 Source Diagnostic Test (SDT) [15, 16, 17]. For this application both steady and well as unsteady RANS simulations have been performed comparing actuator disk, actuator line and sliding mesh methods. The different methods are evaluated comparing accuracy as well as computational costs. A final conclusion is drawn in Section 6.

2 Computational Methodology

The LAVA solver framework [1] is utilized for this computational study. LAVA offers flexible meshing options and was developed with the intent of modeling highly complex geometry and flow-fields. The framework supports Cartesian and curvilinear structured grids as well as unstructured arbitrary polyhedral meshes. However, for this study the structured curvilinear overset approach was chosen. Applications of the LAVA framework being used for several aerodynamic as well as aeroacoustic problems can be found in [18, 19, 20, 21, 22]. For this work, the compressible Reynolds Averaged Navier-Stokes equations are solved using a finite-difference formulation applied to the curvilinear transformed system of equations in strong conservation law form. The Spalart Allmaras (SA) turbulence model [23] is used as a RANS closure model. In the current work, a second-order accurate convective flux discretization is used for the mean-flow equations, consisting of a modified Roe scheme with third-order left/right state reconstruction and a Koren limiter [24]. The turbulence model convective terms are discretized using the first-order upwind

scheme. The linear solver uses an incomplete lower-upper factorization (ILU) preconditioned generalized minimum residual (GMRES) method [25], while the nonlinear solver uses an approximate Newton-Krylov approach. All steady simulations are initialized from free-stream conditions unless otherwise specified, while the pseudo-time step CFL is initiated at 5.0 and is then automatically increased to a maximum value of 1000 as the solution progresses. Simulations were run until the steady-state convergence criteria was met, or until the standard deviation of drag coefficient in nonlinear iteration space falls below 1×10^{-5}. For all grid resolutions simulated, this convergence criteria typically corresponds to 5-6 orders of flow equation residual reduction. Overset grid technology [26] is used to couple the solutions across overlapping meshes. In this study, the structured curvilinear overlapping grid methodology is used. The curvilinear overset grids are generated utilizing the Pointwise$^{\text{TM}}$ and Chimera Grid Tools (CGT) [27] software packages.

This paper examines a comprehensive set of validation test-cases for propulsive models implemented in the LAVA solver framework. The different propulsion models implemented in the LAVA solver are:

- Actuator disk method with constant, linear or user-prescribed loading;
- Actuator line method with constant, linear or user-prescribed loading;
- Sliding mesh method with actual rotor/blade geometry included in the overset grid.

The actuator disk method is generally applied to steady state simulations, while the other two methods are applicable to time-accurate simulations only.

2.1 Actuator Disk Model

The most basic method for modeling the influence of a propulsion element is through the use of an actuator disk. In this approach, a pressure discontinuity is imposed on the flow field. In principle, this represents the case where the number of blades approaches infinity. Although an infinite number of blades is never true in practice, the actuator disk model solutions can be seen as a time-averaged solution of a rotor with a finite number of blades. Actuator disk methods are commonly utilized for steady-state simulations. In the literature, actuator disk methods are usually divided into two categories: a source term-based approach and a pressure/velocity jump boundary condition (BC). The source term approach was initially introduced by Rajagopalan and Fanucci [28]. A comparison of these two approaches can be found in the work by Le Chuiton [29]. Both variations have been implemented within the LAVA solver. However, based on internally conducted analysis, the source term approach demonstrated to be more robust and stable, especially when adding swirl. In addition, the source term implementation is more general as it can be applied to a volume as well as a disk. Therefore, the main focus herein will be on the first approach. Another benefit of the source term method is the ability to spread the disk out over more than 1 cell in the axial direction. This reduces the strong discontinuity introduced through the actuator disk and more closely resembles gradual pressure rise through a rotor. The contributions of the actuator disk source term to the compressible governing equations are as follows:

$$\begin{bmatrix} f_x \\ f_y \\ f_z \end{bmatrix} = \begin{bmatrix} n_{ax,x} \\ n_{ax,y} \\ n_{ax,z} \end{bmatrix} \cdot F_{\text{Thrust}} + \begin{bmatrix} n_{\Theta,x} \\ n_{\Theta,y} \\ n_{\Theta,z} \end{bmatrix} \cdot F_{\text{Torque}} \tag{1}$$

$$\text{RHS} = \text{RHS} + \begin{bmatrix} 0 \\ f_x \\ f_y \\ f_z \\ \vec{f} \cdot \vec{V} \end{bmatrix} \tag{2}$$

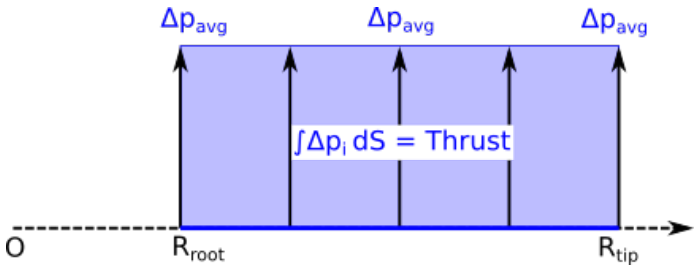

(a) Constant disk loading.

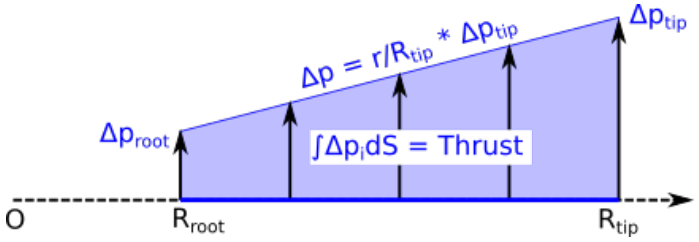

(b) Linear disk loading.

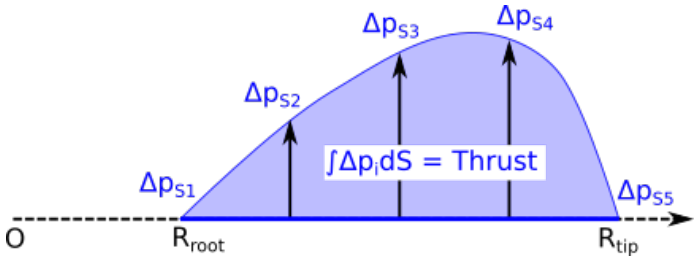

(c) Example prescribed disk loading.

Figure 1: Different actuator disk blade loadings prescribed at each source term location. The prescribed disk loading is applied to every source term location via a curve-fit or volume input file.

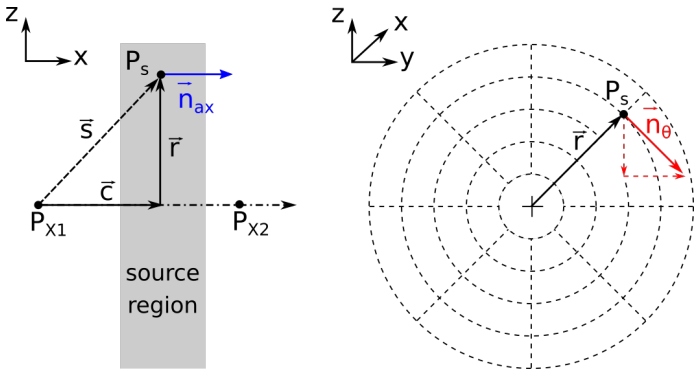

Figure 2: Schematic of computed normalized source direction vectors in axial $\vec{n}_{ax}$ and tangential n_Θ direction. Computation of body-force is performed in a prepossessing step at each of the solution points within the actuator source term region. To obtain the total force applied to the RHS and LHS the normalized source direction vectors get multiplied with the total thrust and torque force: $\vec{f}_{\text{total}} = \vec{f}_{\text{ax}} \cdot F_{\text{Thrust}} + \vec{f}_\Theta \cdot F_{\text{Torque}}$.

$$\text{LHS} = \text{LHS} + \begin{bmatrix} 0 & 0 & 0 & 0 & \\ \frac{\partial f_x}{\partial P} & \frac{\partial f_x}{\partial (u)} & \frac{\partial f_x}{\partial (v)} & \frac{\partial f_x}{\partial (w)} & 0 \\ \frac{\partial f_y}{\partial P} & \frac{\partial f_y}{\partial (u)} & \frac{\partial f_y}{\partial (v)} & \frac{\partial f_y}{\partial (w)} & 0 \\ \frac{\partial f_z}{\partial P} & \frac{\partial f_z}{\partial (u)} & \frac{\partial f_z}{\partial (v)} & \frac{\partial f_z}{\partial (w)} & 0 \\ \frac{\partial \vec{f}}{\partial P} \cdot \vec{V} - \vec{f} \cdot \frac{\vec{V}}{P} & \frac{\partial \vec{f}}{\partial (u)} \cdot \vec{V} + \frac{f_x}{P} & \frac{\partial \vec{f}}{\partial (v)} \cdot \vec{V} + \frac{f_y}{P} & \frac{\partial \vec{f}}{\partial (w)} \cdot \vec{V} + \frac{f_z}{P} & 0 \end{bmatrix} \tag{3}$$

Several different loading options can be chosen for this form of actuator disk implementation. The simplest versions are a constantly loaded disk, followed by a linearly loaded disk. In addition, a prescribed fixed loading can be applied to the disk at each source term location. The latter method is a convenient way of supplying a loading computed with a more sophisticated tool in a preprocessing step. An example depiction of such loading functions can be seen in Figure 1. These loadings are independent of the incoming flowfield, and thus the contributions to the left hand side Jacobian are almost all zero except for the energy equation. In addition, methods that depend on the incoming flowfield, like blade element method (BEM) [30] or a blade loading model (BLM) [31], can also be implemented with this source term method. However, these methods are not considered in this study.

Figure 2 depicts how the source term contributions are computed within the source term method. This applies to both the actuator disk/volume as well as actuator line method. The computation of the directional vectors in the azimuthal as well as axial direction for each actuator solution point is performed *a priori* to the simulation utilizing simple vector algebra and consists of the followings steps:

- Axial force direction: $\vec{f}_{ax} = \frac{P_{x2} - P_{x1}}{|P_{x2} - P_{x1}|}$
- Vector from rotational axis start point P_{x1} to source points P_{S}: $\vec{s} = P_S - P_{x1}$
- Projected length of s onto centerline axis: $|\vec{c}| = \vec{s} \cdot \vec{f}_{ax}$
- Radial vector from centerline to source point: $\vec{r} = \vec{s} - |\vec{c}|\vec{f}_{ax}$
- Azimuthal force direction using right-hand rule: $\vec{f}_\Theta = \vec{f}_{ax} \times \vec{r}$

2.2 Actuator Line/Blade Model

The blade loading method is in principle the same as the actuator disk method, with the difference of a time-dependent source term. Here, instead of distributing the load over the entire disk as a time-averaged force, we use a Gaussian projection function along a 1D line representative for each blade. This method has

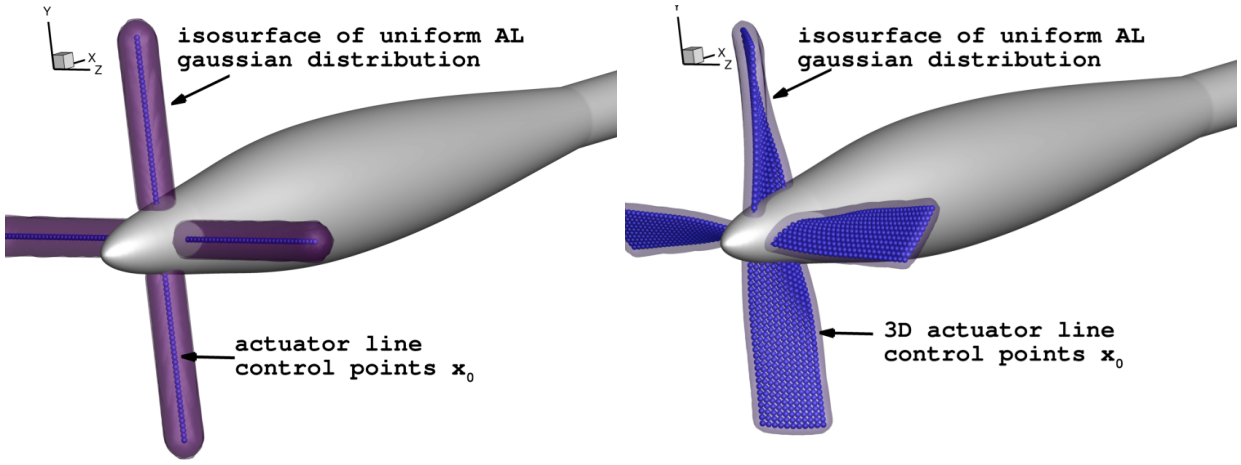

(a) 1D control points

(b) 3D control points

Figure 3: Isosurface of actuator line Gaussian distribution for a four blade tip-mounted rotor mounted on a nacelle. Blue spheres represent the actuator line control points used in the distribution function for (a) 1D line control points (b) 3D control points representing blade twist.

initially been outlined by Sorensen and Shen [32], where a three-dimensional Gaussian with isotropic width is applied. The function is given by

$$\Phi(x,y,z) = \frac{1}{\epsilon^3 \pi^{3/2}} \exp\left(-\frac{(x-x_0)^2+(y-y_0)^2+(z-z_0)^2}{\epsilon^2}\right), \tag{4}$$

where x, y and z are the coordinate directions, the subscript 0 describes the location of the actuator line control points around which the Gaussian is applied and ϵ is the Gaussian width. In order to obtain the actuator line (AL) body-force, one multiplies the thrust and torque forces with this Gaussian filter function $\vec{f}(x,y,z) = \Phi \cdot (\vec{F}_{thrust} + \vec{F}_{torque})$. The resulting cylindrical tube is depicted in Figure 3, which shows the iso-surface of the projection function Φ applied to the tip-mounted configuration of [13]. This method is very sensitive to the choice of the isotropic Gaussian width. Guidance is given in the literature for multiple applications [33, 34, 35, 32]. However, this choice is heavily dependent on the blade geometry and grid resolution, with values typically ranging from 0.2 to 0.035. It has been shown that a constant Gaussian width along the span can also lead to over-prediction of the tip loads. As a solution, a varying width along the span has been proposed by Jha *et al.* [36]. An alternative solution which not only varies the projection function in span but all three coordinate directions is given by Sorensen and Shen [32]. This distribution resembles the shape of an actual rotor more closely. This results in a projection function of the form

$$\Theta(x_c,x_t,x_r) = \frac{1}{\epsilon_c \epsilon_t \epsilon_r \pi^{3/2}} \exp\left(\frac{(x_c-x_{c,0})^2}{\epsilon_c^2} - \frac{(x_t-x_{t,0})^2}{\epsilon_t^2} - \frac{(x_r-x_{r,0})^2}{\epsilon_r^2}\right), \tag{5}$$

where x_c, x_t, x_r are the coordinates in the chord-wise, thickness-wise and radial directions respectively. Both the isotropic distribution function with varying width in span, as well as the non-isotropic Gaussian Θ, are implemented into the LAVA solver. In addition the non-uniform Gaussian distribution method was further extended by replacing the 1D control point line for each blade with a point cloud in 3D space. This is of particular benefit for blade geometries which have significant twist typical for internal propulsion cases (see Figure 3b), resulting in a source term distribution that more closely resembles the actual blade geometry. However, due to the increased amount of control points this approach is computationally more expensive. As this process is only performed during the prepossessing step, it won't have any impact on the final simulation time.

2.3 Sliding Disk Method

The highest fidelity of the rotor methods considered is the sliding disk approach. In this method, the full geometry of the rotor is modeled and the blade physically rotates at the desired RPM. The sliding mesh approach enables efficient communication between rotating and fixed geometry. The approach implemented in LAVA uses an initial grid that forms a point-matched block-to-block connection at the sliding interface. As one (or both) of the meshes rotate, a given node on the boundary will follow a "ring" of nodes on the other mesh. This greatly simplifies the required interpolation as only a 1-D interpolation in θ space needs to be performed. An example of such a sliding interface can be seen in Figure 18(d) applied to the R4 STD geometry. The sliding mesh method has initially been introduced by Rai [37] in 2D and later been extended for 3D [38]. More recent papers were published by Wang *et al.* [39] and Ramirez *et al.* [40].

3 Verification and Validation

3.1 Isolated Rotor - Validation with Momentum Theory

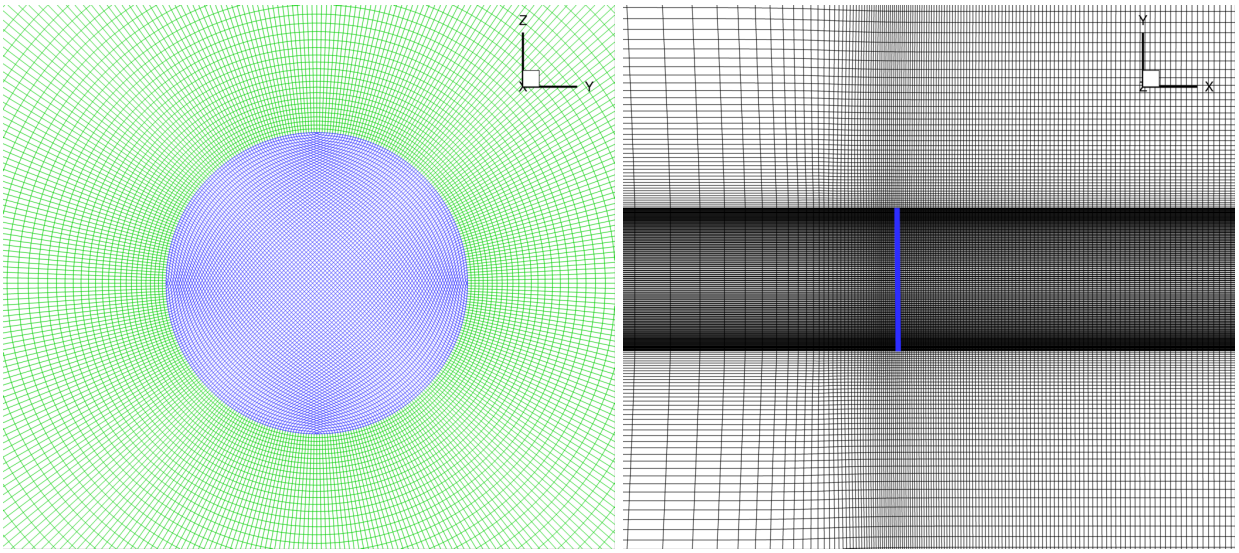

(a) x/R = 0. (b) z/R = 0.

Figure 4: Depiction of mesh for isolated rotor case. (a) O-H mesh topology with actuator region H-mesh in blue and far-field O-mesh in green. (b) displayed clustering in streamwise direction and towards actuator disk tip.

First, the implementation is tested against a theoretical rotor and compared with a 1D analytical solution from momentum theory. For this theoretical rotor with a constant uniform loading, the velocity far downstream of the disk amounts to twice the induced velocity. Such a validation is performed in Bettschart [41], and results from this simulation are compared with RANS performed by O'Brien [42]. However, before simulating the case with a loaded disk, a through-flow simulation was conducted with zero loading. For this simulation the L^2 residual norm instantly reduced to machine precision. This serves as a validation that the specific actuator disk mesh does not introduce any additional errors. Even though any arbitrary thrust could be chosen, a value of $T/A = 299.73\,\mathrm{N\,m^{-2}}$ was selected in order to match the conditions used experimentally. This results in a theoretical velocity induced at the far-downstream centerline of $11.16\,\mathrm{m\,s^{-1}}$. The simulation has a non-dimensional blade radius of one and the domain extends 50D in the streamwise and radial directions. The mesh consists of an H-type block at the actuator disk with 91×91 nodes and extends towards an O-Type far-field using 30 points with a stretching factor of 1.1. The number of points in the

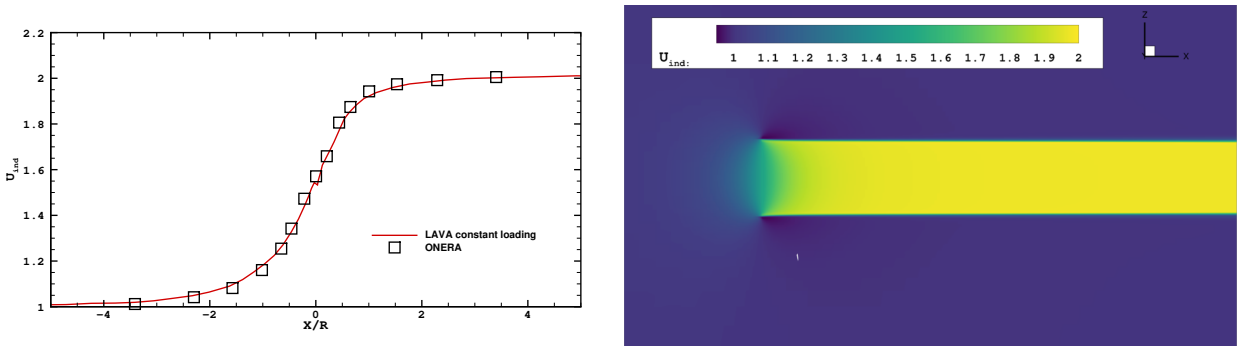

(a) Velocity along centerline.

(b) Contour plot of induced velocity at Y = 0.

Figure 5: Comparison of computed normalized velocity with reference [41].

Table 1: Flow and propeller conditions.

Parameter	Value
Rotor Radius R	0.4572 m
Rotor cutout	2.7%
Rotor inner Radius R_i	$0.027R$
Fuselage Diameter D	$0.2931R$
Fuselage Nose Radius r	$0.1465R$
Fuselage Length (estimated) L	$3.0R$
Fuselage Angle of Attach α	0°
Rotor Hub Location X_0/Z_0	$1.0R$ / $0.3R$
Rotor Shaft Angle	−6.0°
Rotor speed n	2,100 rpm
Reference length L	$3.0R$
Reynolds number $\mathrm{Re_L}$	0.9196×10^6
Mach number M_∞	0.0295
Thrust Coefficient C_T	0.009045
Advance ratio $J = U_\infty/(n \cdot 2\mathrm{R})$	0.1

streamwise direction is 200, with a clustering in the region $1R$ upstream and $5R$ downstream of the actuator disk. The mesh is depicted in Figure 4. Simple 1D propeller theory based on momentum, Bernoulli and continuity equations applied for incompressible flows can be found in [43]. For comparison, the normalized velocity U_{ind} is defined as follows, with U_F being the Froude velocity:

$$U_{ind} = \frac{1}{2}\frac{U - U_{ref}}{U_F} + 1 \ , \tag{6}$$

$$U_F = \frac{1}{2}\left[\sqrt{U_{ref}^2 + \frac{2\Delta p}{\varrho}} - U_{ref}\right] \ . \tag{7}$$

Figure 5(a) shows the computed normalized velocity along the centerline. Good agreement with theory and results from [41] can be observed.

3.2 Validation for Top-Mounted Applications

The Georgia Institute of Technology (GIT) Rotor-Airframe Model was used as the second validation case and is depicted in Figure 6. The configuration consists of a cylindrical body with a hemispherical nose. The dimensions of the configuration and flow conditions can be found in Table 1. The rotor is tilted 6°

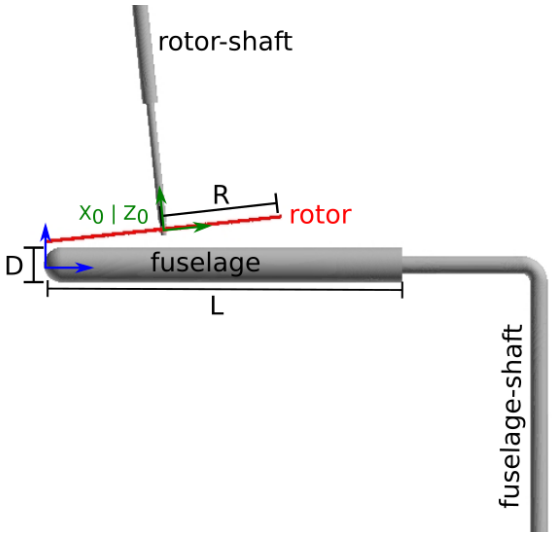

Figure 6: Georgia Tech Rotor-Airframe Model setup [42]

forward and has a cutout of 2.7 %. The rotor in the experiments is modeled with two untwisted NACA-0015 plan-form airfoil sections. The model has been extensively tested in the GIT John J. Harper 7ft. $\times$9ft. wind tunnel and details can be found in multiple studies [12, 44, 45, 46]. In addition, several computational studies have been performed using various propulsion models of differing fidelity's [47, 42, 14].

The rotor is operated at 2,100 rpm, with a thrust coefficient of 0.009 045. A zero degree angle of attack with a Mach number of 0.029 and a Reynolds number based on the fuselage length (3R) of 9.196×10^5 was chosen. The following two configurations were created: a configuration without rotor/fuselage-sting and a configuration with simplified rotor-sting. Details of the geometric simplifications can be found in O'Brien [42]. An overset approach was chosen for the rotor mesh with 181 points in the rotor's azimuthal direction. The total number of grid points is 3×10^6. As a first case, simulations were performed without the rotor powered on for the two configurations. The pressure coefficient distribution is shown in Figure 7(a). The inclusion of the simplified sting, which only consists of a cylinder, seems to be necessary in order to correctly predict the loads on the fuselage. As shown in O'Brien's thesis, varying the shaft from a simplified geometry to something that resembles the experiment more closely will improve this even further. However, as the main focus of this paper is not on tip-mounted applications this will not be investigated further and the reader is referred to O'Brien's thesis. Finally, two powered cases were simulated with a constant and a linear disk loading and pressure distributions along the fuselage top centerline plane are plotted in Figure 7(b). Overall a good agreement can be observed with the linear loading. The constant loading shows a significant over-prediction at the centerline and misses the peaks towards the rotor tip. The slightly larger pressure at the center of the rotor axis at $X = 1R$ can also be attributed to the missing complex sting in the configuration. However, we demonstrate that when choosing an appropriate load distribution the actuator disk method gives a reasonable approximation for a top-mounted rotor-craft while being computationally significantly cheaper than modeling the rotor in a time-resolved simulation procedure.

3.3 Validation for Tip-Mounted Rotor Applications

This case considers the interaction of a propeller with a simplified hub/fuselage and wing. For this study, the experiments of Samuelsson [13] were considered. This is representative of turboprop aircraft and novel distributed electric propulsion system concepts such as those found in NASA's X-57 Maxwell airplane [48, 49] (see also Section 4). For this work, two specific configurations are considered: first, an isolated propeller mounted on a hub/fuselage; secondly, a case that includes a wing mounted at the side of the hub/fuselage to investigate the rotor wake-wing interaction. Comparisons are made with steady state RANS using the actuator disk method with different loading types. This case has been previously studied by Guzel et. al [14] for the implementation of actuator disk methods within a RANS solver framework. Additional inves-

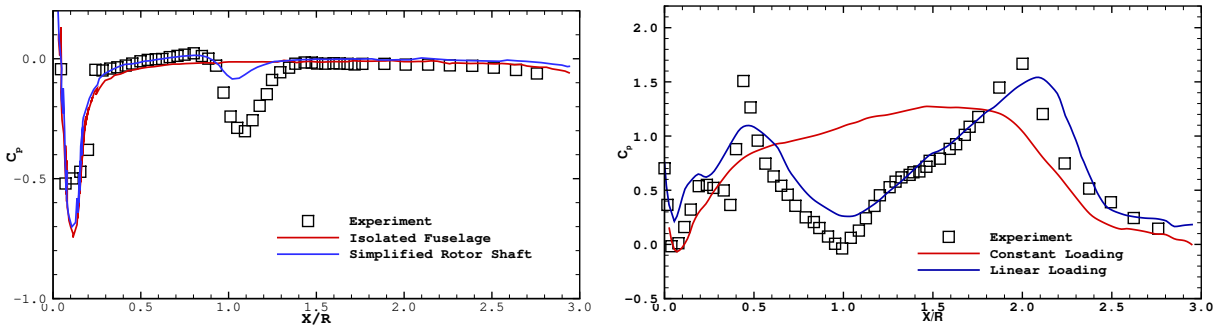

(a) Rotor powered off.

(b) Rotor powered on.

Figure 7: Pressure coefficient distribution on fuselage of GIT with and without rotor power.

Table 2: Flow and propeller conditions.

Parameter	Value
Advance ratio J	0.705
Reference length L	1.672 m
Reynolds number Re_L	1.7×10^6
Mach number M_∞	0.15
Reference Velocity	$50\,\mathrm{m\,s^{-1}}$
Thrust Coefficient C_T	0.23
Power Coefficient C_P	0.23

tigations to observe actuator disk methods in an inviscid Euler solver have been performed by Thom and Duraisamy [50, 10]. Several publications using unsteady RANS including the full blade geometry or a variation of a similar rotor have been performed in the literature [51, 52, 10], making this an ideal case for the validation of actuator disk for turboprop applications. The experimental setup is displayed in Figure 8(a). The configurations corresponds to case 1 (hub/fuselage only) and case 2 (hub/fuselage + wing) from experiment bt Samuelsson *et al.* [13]. The wing consists of a constant NACA63_{010}A012 airfoil section with a chord of 0.5 m and a semi-span of 1.0 m mounted at the centerline, 0.435 m downstream of the rotor axis origin. The rotor in the experiments has a diameter of 0.64 m and is representative of a modern medium speed turboprop commuter aircraft operated at high thrust. Pressure distributions along the centerline are supplied for both cases with and without wing, as well as for propeller on and off configurations. However, it should be noted that for the configuration with propellers turned off, the 4-bladed rotor was still mounted to the configuration. This will result in a smaller difference of the pressure distribution compared to the case without the rotor. The experimental flow conditions are summarized in Table 2.

Firstly, simulations were performed for the hub/fuselage configuration without wings (Configuration 1) with and without actuator disks. A comparison between pressure coefficient plots can be seen in Figure 9(a). Results along the centerline symmetry plane are compared both with experimental results [13] as well as a RANS simulation performed by Guzel et. al [14]. A good agreement has been observed. The deviation between the LAVA results and the ones shown by Guzel are from differences in how the geometry is treated towards the end of the hub/fuselage. In this study the hub/fuelage was extended towards the end of the computational domain in order to represent the mounting sting present in the experiments. In contrast, Guzel ended the hub/fuselage with a blunt trailing edge. This results in larger pressure values due to the change in slope where the hub/fuselage transitions into the sting. The deviation from experiments in the near-nose region is likely due to the fact that the experiments never removed the propeller, while the propeller was absent in this particular simulation. In a second step, simulations were performed for a constant, linear and linear loaded disk with added swirl. For these simulations, a power coefficient of $C_T = 0.2435$ was used. Results for the pressure over the hub/fuselage can be seen in Figure 9(b). The constantly-loaded disk shows an over-prediction across the hub/fuselage surface. Switching to a linearly distributed loading seems

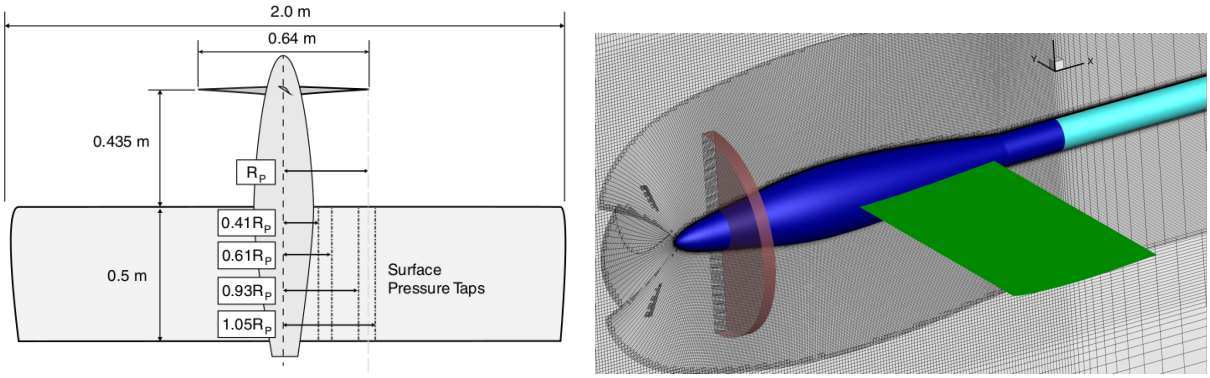

(a) Experimental setup.

(b) Geometry and mesh.

Figure 8: Depiction of experimental setup from Samuelsson [13] (a) and mesh used (b). Area of actuator disk/volume highlighted in red, hub/fuselage with sting extension in blue and wing in green.

to significantly improve these results. However, an over-prediction towards the hub/fuselage nose is still observed. Further improvement could be observed for the leading edge of the hub/fuselage when including a swirl velocity in the actuator disk method. Overall good agreement with experiments and other CFD codes have been shown and demonstrated for Configuration 1.

Secondly, simulations and comparisons for Configuration 2, which include the rotor wake-wing interaction, were performed. For this case, in addition to pressure plots along the centerline, pressure plots along sections of the wing are provided. The pressure cuts along the wing are displayed in Figure 8(a). The same comparisons along the centerline was made for both propeller on and off configurations and are depicted in Figure 9(c) and 9(d). A linear loading with added swirl was chosen for the power-on configuration as this has shown to agree with experiments the best. A satisfactory agreement with experiments was achieved. For the powered case a clear effect of the swirl can be observed where it results in a up- and down-wash effects on the wings. This results in increased and decreased pressure distributions on the wing leading edge. The effect of the propeller slipstream induced by the swirl can be observed across the different c_p cuts along the wing shown in Figure 10. A good agreement with experiments was achieved. The c_p line-plots observed are displayed on the right wing which sees an up-wash effect from the swirl induced by the rotor. This validation case shows that actuator disk methods can successfully capture the effect of rotor-wing interaction on a simplified problem. However it has also shown that a more sophisticated choice of load distribution will result in significantly improved results compared to experiments. Even when switching from a constant loading to a linear loading major improvements were achieved. Additional methods to obtain a even more sophisticated loading distribution were utilized and are further discussed in Section 5.4.

4 Tip-Mounted Propulsion Application: NASA X-57 Maxwell Electrified Aircraft

4.1 Problem Description

The LAVA team, in collaboration with researchers at NASA Langley and NASA Armstrong Research Centers [49, 53], was tasked to populate aerodynamic databases that contained aerodynamic coefficients computed for the X-57 Maxwell aircraft. Ultimately, CFD predictions would serve to construct lower order aerodynamic models for system level analysis, as well as develop a flight simulator used to train pilots to handle a variety of nominal and off-nominal conditions. Therefore, it was necessary that these simulations would cover conditions that span the flight envelope of the X-57, including the propulsive effects at various power settings throughout a typical mission as well as during failure scenarios. The X-57 leverages distributed electric propulsion technology, which includes 12 high-lift propellers distributed across the span of the wing

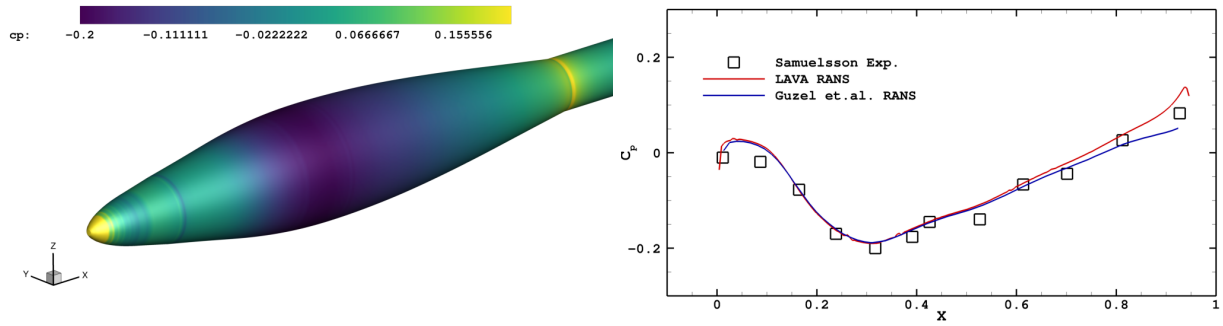

(a) hub/fuselage - power off

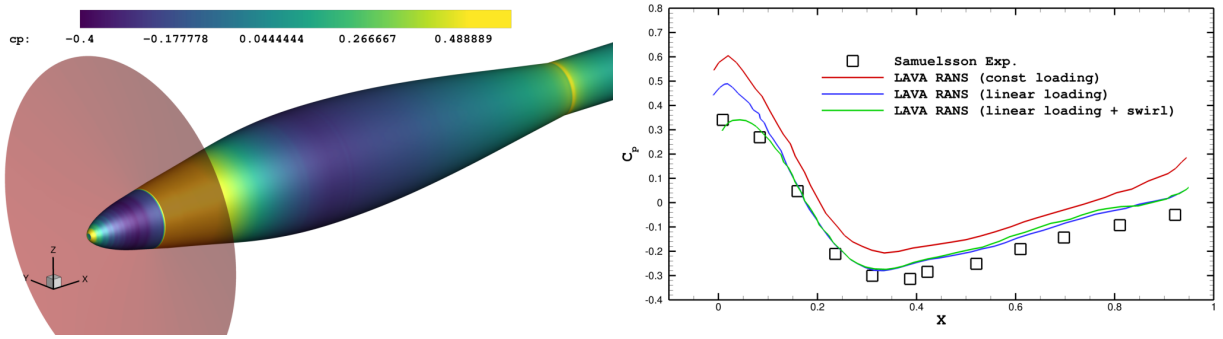

(b) hub/fuselage - power on

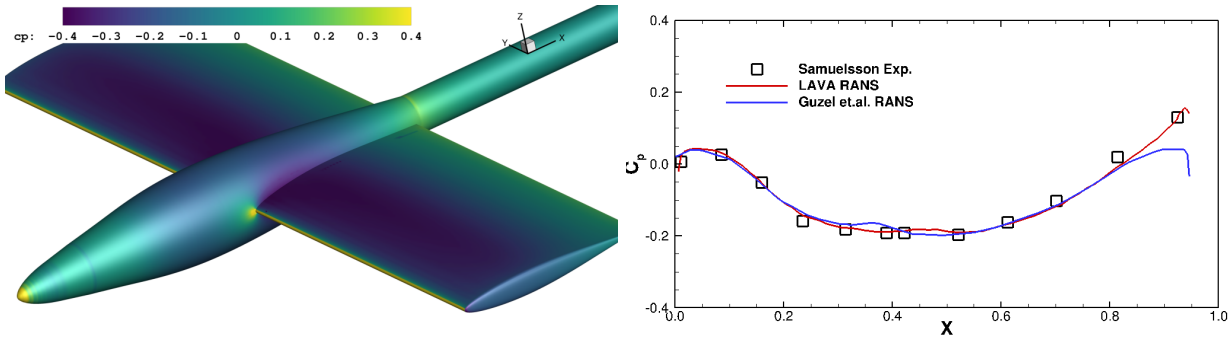

(c) hub/fuselage + wing - power off

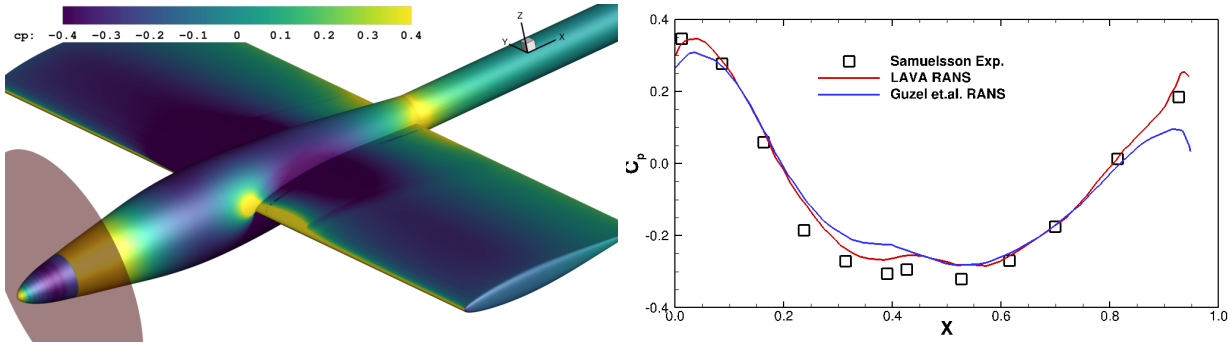

(d) hub/fuselage + wing - power on

Figure 9: Pressure coefficient *cp* contour plot (left) and c_p along the hub/fuselage centerline (right). Comparisons made with experiments in [13] and similar RANS performed by Guzel et. al [14].

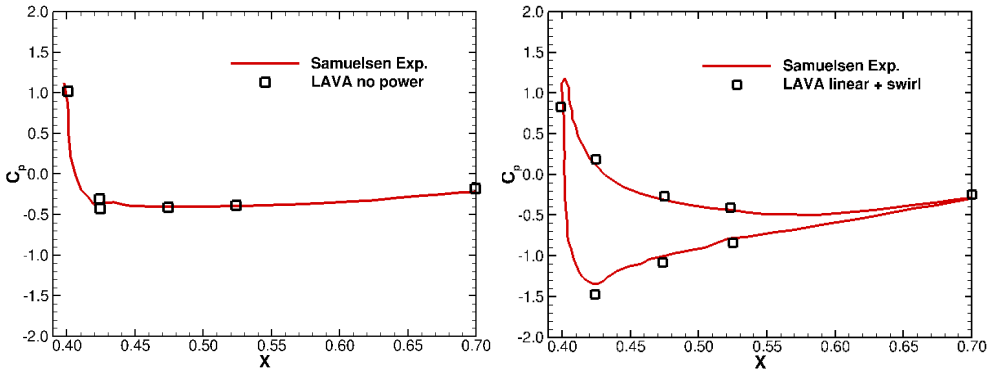

(a) power off: y = 130mm (b) power on: y = 130mm

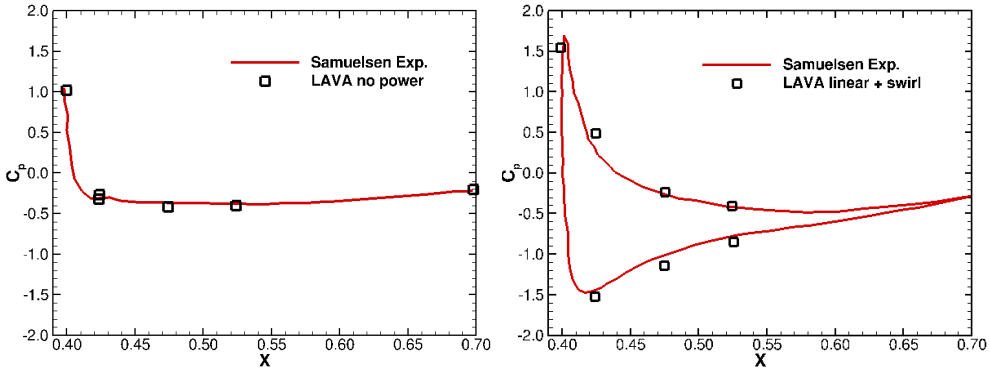

(c) power off: y = 195mm (d) power on: y = 195mm

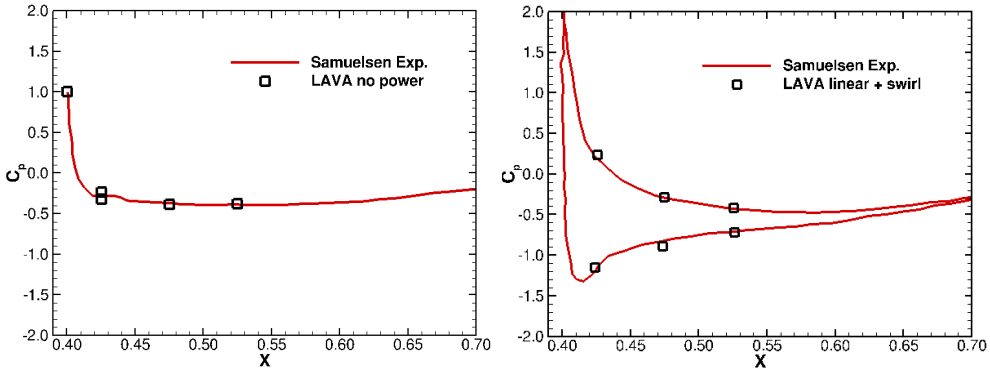

(e) power off: y = 260mm (f) power on: y = 260mm

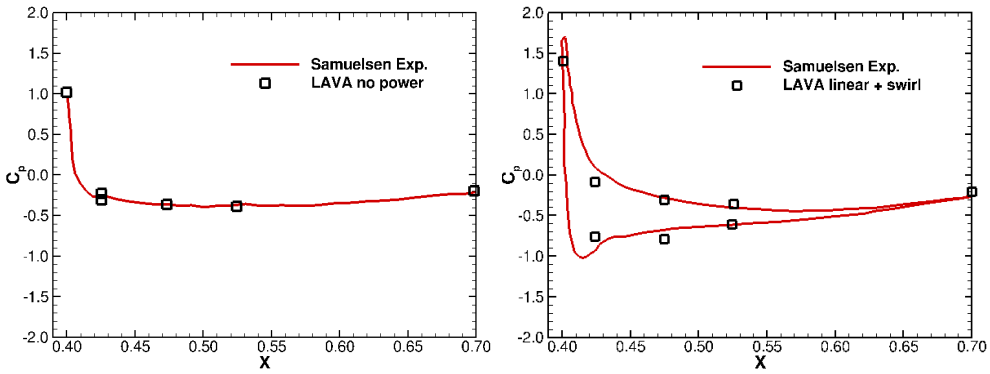

(g) power off: y = 300mm (h) power on: y = 300mm

Figure 10: Pressure coefficient c_p over the wings for powered and un-powered configuration. Comparisons made with experiments in [13].

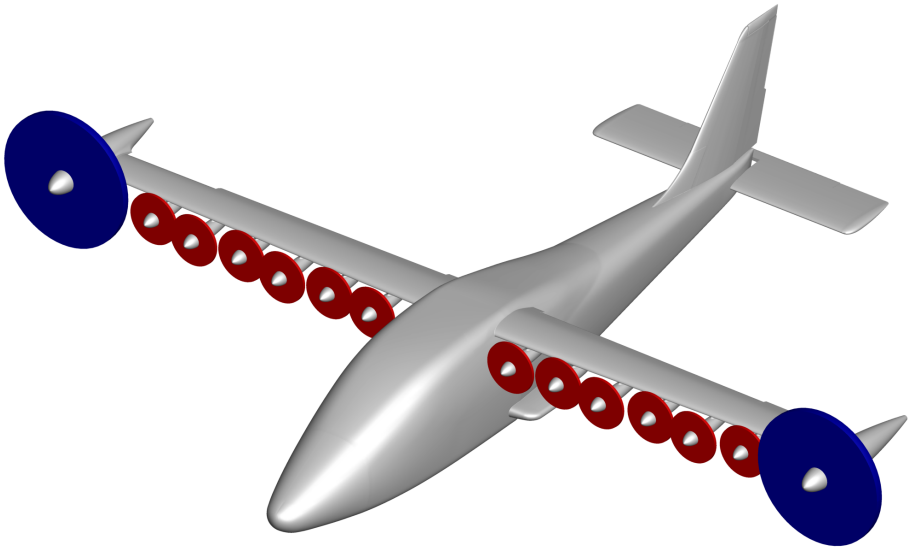

Figure 11: Schematic of the X-57 geometry, with high-lift propulsor actuator regions shown in red and cruise propulsor actuator regions shown in blue.

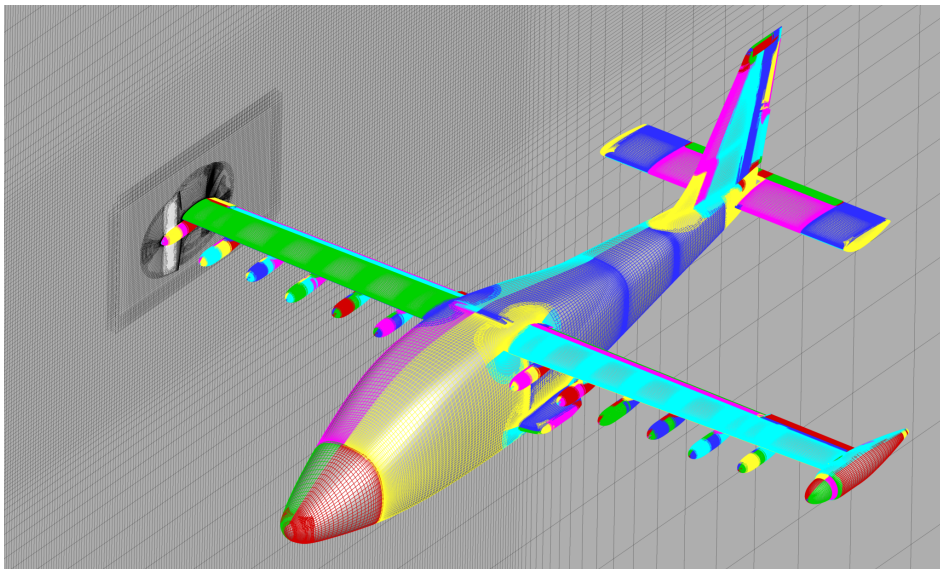

Figure 12: X-57 grid system used for simulating the 30° flap deflection setting with all other control surfaces neutral. Volumetric slice emphasizes an actuator zone shown in white with surrounding body-fitted and off-body domains shown in grey.

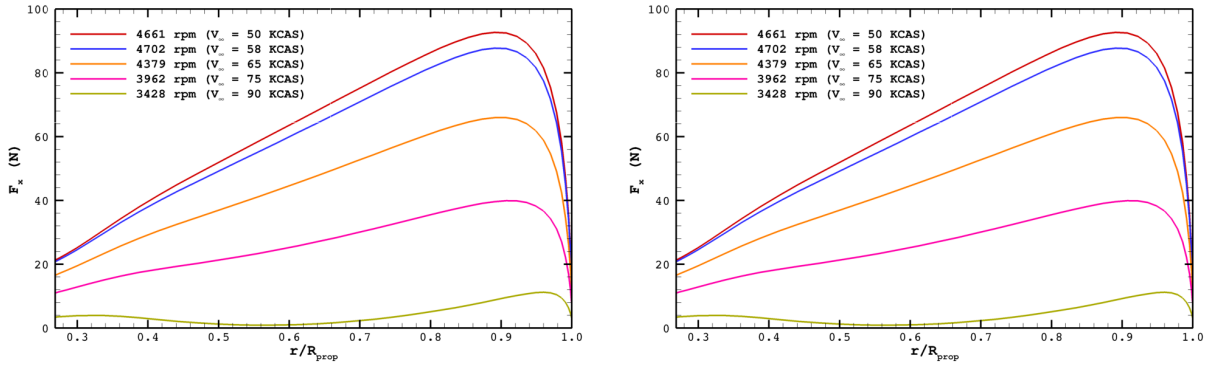

(a) Axial force (thrust).

(b) Tangential force (torque).

Figure 13: Sample actuator zone radial distributions of force for the high-lift propulsors. Thrust and torque are illustrated in (a) and (b) respectively for all power settings required to populate the high-lift database.

as well as two tip-mounted propellers. The former are activated only during takeoff and landing scenarios to maximize lift, while the latter produces the thrust required during the cruise phase. Figure 11 illustrates the X-57 geometry, with the annular region swept out by the high-lift and cruise propulsors denoted. Although not discussed here, multiple studies that validate simulation choices against experimental data for the X-57 are discussed at length in [48]. A simplified approach to modeling propulsion is crucial to maintain a feasible computational cost when simulating the propulsive effects, while simultaneously capturing the dynamics of the rotating blades as accurately as possible. Therefore, this study was deemed a viable candidate to utilize actuator zone modeling in lieu of unsteady rotating blade simulations, which permitted a cost-effective steady RANS approach to be utilized throughout the database generation process. To maximize accuracy of this modeling technique, custom thrust and torque radial distributions shown in Fig. 13 were derived from simulations of the high-lift and cruise blades using XROTOR [54]. These distributions generally exhibit similar qualitative tendencies regardless of the power setting under simulation, however the shift in peak force at low power settings is important to capture, particularly at near-stall conditions where RANS solution sensitivity is most pronounced [55]. Various actuator zone treatments near $C_{L_{\max}}$ were explored in [56] and demonstrate that separation patterns at high angles of attack are dependent on the distribution used, while changes in integrated quantities by up to 5% are also possible at lower angles of attack. The following sections discuss additional computational considerations including mesh generation techniques and sample results from powered database analysis.

4.2 X-57 Overset Curvilinear Grid Generation

Many well-established mesh generation techniques were used to generate the structured curvilinear grid systems throughout this analysis [57]. The geometric complexity of the X-57 resulted in many months of required labor, which was further complicated by the need to articulate deflecting control surfaces. However, once the initial grid systems were completed and grid convergence studies would determine appropriate resolution, many component grids could be reused for future analysis. Additionally, a procedure was developed to automatically deflect control surfaces to a desired setting, allowing for quick turnaround time with minimal manual intervention. While the resulting grid system size depended on the control surface configuration, particularly the flap setting, all database solutions were generated on a grid containing 160 to 180 million solve points. Local clustering of grid points was deemed necessary near various components such as the high-lift pylons, where spanwise distributions were adjusted to properly resolve wakes emanating from the pylons and the actuator zones. The final grid system included over 350 body-fitted overlapping structured zones required to discretize the geometry and surrounding domain and an additional 12 Cartesian zones that would interface with the far-field. Far-field boundaries treated with a Riemann invariant boundary condition were placed sufficiently far from the vehicle at 1,000 body lengths to ensure boundary placement would not

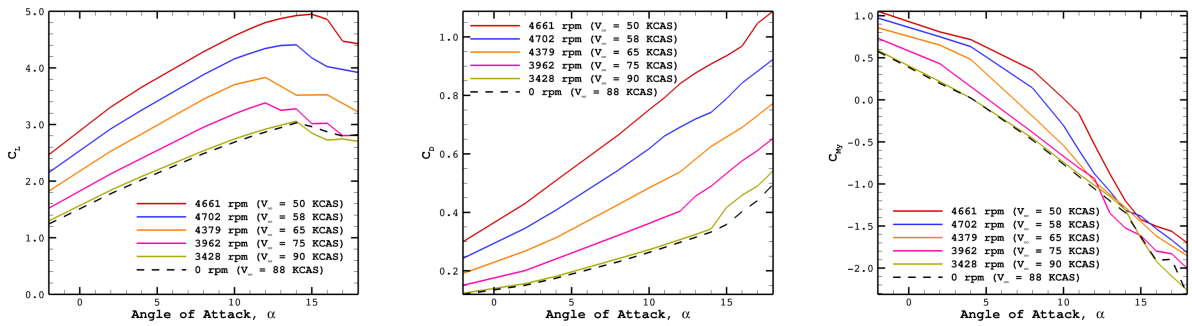

(a) Lift (b) Drag (c) Pitching moment

Figure 14: Sample integrated quantities for powered simulations at the 30° flap setting for 10° angle of attack.

impact the near-field solution.

Proper incorporation of the actuator zone grids was an important consideration while developing powered databases. Apart from the actuator zones themselves, higher resolution Cartesian grids were also inserted aft of these regions to ensure downstream effects could be properly resolved. This was deemed necessary as higher flow field gradients would be introduced with applied propulsion, and solution sensitivity was observed depending on the treatment of these regions. A sample grid system is depicted in Fig. 12, with a volumetric slice shown at a sample actuator zone location. The same grid system would be used for all cases simulating a fixed aircraft configuration, regardless of freestream condition or propulsor setting.

4.3 Sample Database Solutions for the X-57

Since the X-57 database generation study was primarily concerned with quantifying the change in aerodynamic loading for powered cases relative to unpowered results, many comparisons were made between various power settings. This not only involved comparing integrated quantities at various conditions, but also entailed studying flow field visualizations to understand the underlying physics that governs aircraft performance. Figure 14 compares aerodynamic coefficients across the range of angles of attack simulated for the 30° flap setting with all high-lift propulsors functioning normally.

Results suggest that applying maximum power to the high-lift propulsors nearly doubles the lift generated relative to an unpowered condition, while simultaneously doubling the integrated drag. This is primarily driven by a substantial drop in wing suction side pressure due to the accelerated flow and resulting lift-induced drag. Applying power to the propulsors also tends to delay stall by up to 3° when comparing to the lower power settings. Since the added momentum serves to keep the flow over the wings attached at high-α conditions, the lift curves at higher power settings continue to increase at higher angles of attack, although tend to flatten out to produce a much less pronounced break. The slope of the powered $C_{L\alpha}$ and $C_{D\alpha}$ curves is also influenced by the addition of propulsion, which remain essentially constant regardless of the power setting. Therefore, changing angle of attack with propulsion applied is predicted to produce a greater change in aerodynamic loading as compared to an unpowered condition. With respect to pitching moment, application of power tends to produce an increased nose-up pitch tendency until near-stall conditions are reached, at which point all predictions tend to coalesce. This decreased sensitivity in pitching moment at higher angles of attack is primarily due to the reduced downwash effects on the horizontal stabilizer, which is responsible for the vast majority of total pitching moment. As the freestream velocity vector is rotated to a sufficiently high angle of attack, the downstream impact of the propulsors tends to bypass the tail section from above, thereby resulting in a tail loading that resembles an unpowered condition.

To illustrate the actuator zone effects on the surrounding flow field, Fig. 15 provides a visualization of local streamwise velocity for various power settings at 10° angle of attack. Although the same thrust and torque is applied to all high-lift propulsors, the qualitative nature of the downstream wakes is unique, particularly

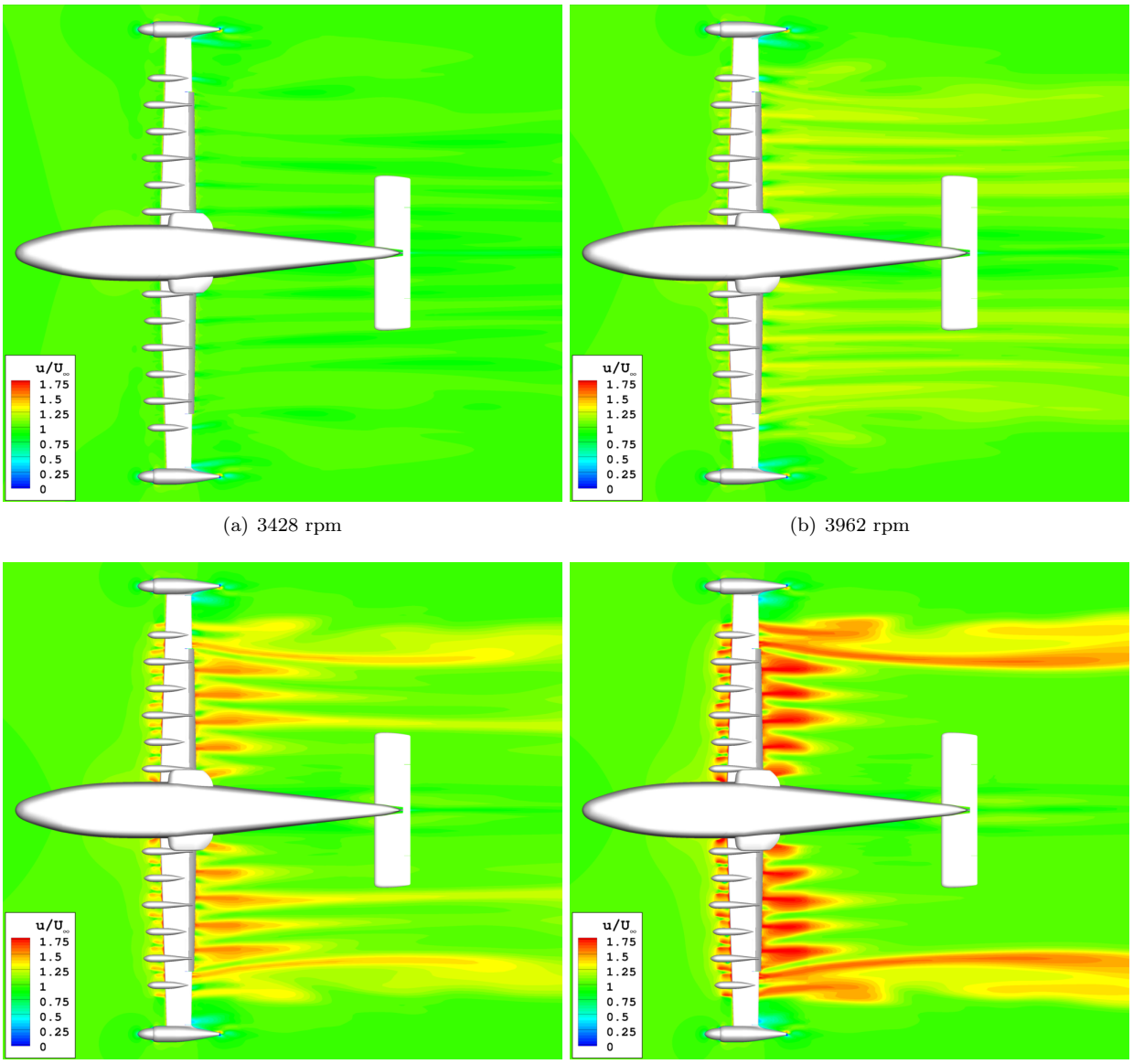

(a) 3428 rpm

(b) 3962 rpm

(c) 4379 rpm

(d) 4702 rpm

Figure 15: Streamwise velocity distributions shown for various high-lift propulsor power settings.

at the highest power settings. This is believed to be primarily attributed to the geometric differences in the vicinity of each high-lift pylon, which interact uniquely with the momentum increase produced by the actuator zone. In particular, the unobstructed flow at the outboard-most high-lift propulsor locations allows the induced momentum to persist much further downstream than the high-speed flow produced by the inboard propulsors. Additionally, at higher angles of attack, inboard wing corner flow separation as well as separation between various high-lift pylons also tends to influence the high-momentum propulsor wakes, a phenomenon that begins to arise at the angle of attack shown.

Future work might study the effects of a higher resolution grid in these actuator wake regions and the upstream impact this would have on the airframe since the flow is incompressible in nature. However, with thorough code-to-code comparisons and verification and validation studies, confidence was built that actuator zone modeling provided the fidelity necessary to predict powered aircraft performance.

5 Internal Propulsion Application: NASA R4 Source Diagnostic Test (SDT)

5.1 Problem Description

A final application case study for the actuator disk and actuator line models within the LAVA solver framework will be presented in this section. Data obtained at the NASA Glenn Research Center from the Source Diagnostic Test (SDT) case will be utilized for this purpose [15, 58, 16, 17]. This test-case was also used for acoustic-noise prediction during the AIAA Fan Broadband Noise Prediction Workshop [59]. The dataset contains relevant data not only for noise computation validation (which is outside the scope of this work), but also for aerodynamic quantities such as mean and root-mean-square (RMS) turbulent velocities obtained via hot-wire measurements downstream of the rotor stage. Therefore, it is a valuable dataset for the validation intended in this work. In addition, the SDT test case has been studied extensively, and several publications focused on the fan noise computations are available in the literature. Shur et al. [60, 61, 62] used two different methodologies to compute both tonal and broadband noise generation/propagation in the fan rig. Unsteady RANS (URANS) and a zonal approach combining both URANS and improved delayed detached-eddy simulation (IDDES) were compared with experiments, and the drawbacks of the former in predicting the mean and unsteady characteristics of the flow were identified. The Lattice Boltzmann Method (LBM) has also been applied to the SDT test case [63] using very large-eddy simulation (VLES), showing a strong agreement with experiment. Finally, the SDT case has also been used for validation of a body force model for propulsor simulations in Overflow [64].

Actuator disk and actuator line methods will be compared against unsteady RANS solutions obtained using a sliding mesh methodology, where the R4 rotor blade geometry is represented fully in the computational domain using a combination of structured overset and multi-block body-fitted grids. All three simulation methodologies will be compared with experimental data and with each other, so as to address their corresponding advantages and drawbacks based on relative cost and accuracy metrics. Comparisons between the three computational methodologies will also be presented at locations where no aerodynamic experimental data is available, with the intent to build an expectation database for each of the three distinct levels of blade modeling accuracy, and point out differences and similarities between methods.

Figure 16 shows an overview of the fan rig geometry for the SDT test case. The 22 in diameter rotor, designated R4, is mounted on a rotating spinner (light gray in Figure 16 that connects to the centerbody geometry. The wind tunnel experiments used a short extension of the centerbody to connect the sting to the wind tunnel walls, whereas in the computational model created for this validation study the constant-area cylindrical section to the right in Figure 16 is extended downstream into the far field. The baseline outlet-guide-vane (OGV) design variant, consisting of 54 blades affixed to the centerbody, is used throughout this study. The nacelle and centerbody components are axisymmetric, and both the rotor and OGV blades are equally spaced. Finally, the tip gap between the rotor blades and the nacelle casing is about 0.5 mm.

In the present work, only the low-speed approach operating condition will be considered, corresponding to a fan rotational velocity of 7808 rotations per minute (RPM), or 61.7 % of the design speed. At this low-speed condition, the rotor tip Mach number based on the freestream speed of sound is about 0.6693. The wind tunnel freestream Mach number is $M_\infty = 0.1$, representative of takeoff and landing conditions. Standard

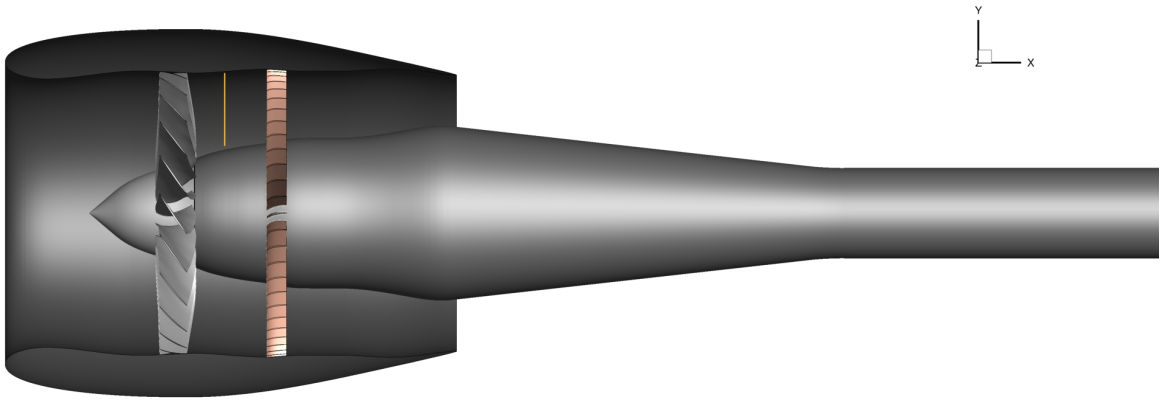

Figure 16: Overview of the SDT geometry with the R4 rotor and baseline outlet-guide-vane (OGV) stages. The light gray surfaces in the centerbody nose (spinner) and rotor represent the rotating components. This rotation is counter-clockwise looking in the +X direction. The yellow line represents the location where single-point hot-wire probe measurements were taken to characterize the rotor wake flow field [58].

sea level conditions are used for pressure and temperature in the far field (p_∞ =101 325 Pa, T_∞ =288.15 K). Adiabatic viscous wall boundary conditions are assumed throughout the domain walls.

To characterize the flow field downstream of the rotor, single-point hot-wire probe measurements of the flow field at station $x = 0.1016$ m were collected during the experimental campaign [58]. This location is indicated by the yellow line in Figure 16. This dataset contains axial, tangential and radial velocity data acquired at a sampling rate of 200 kHz for a duration of 1 second, providing around 129 fan revolutions of velocity data. Additionally, overall fan stage performance results are compiled in [15] for the complete fan stage with the OGVs. Both of these datasets will be used to assess the accuracy of each model in predicting the internal flow field.

5.2 Overset Grid Generation and Computational Setup

The overset grid paradigm was used to create three different grid systems for the simulations proposed. The largest of these grids, used in the context of the sliding mesh simulations (and, therefore, labeled Sliding Mesh grid, or SM grid), encompasses the body-fitted grids representing all components (centerbody, nacelle, OGV and rotor) plus the far field Cartesian boxes that stretch to the boundaries of the computational domain.

The remaining two grid systems, used in the context of the Actuator Disk (AD) and Actuator Line (AL) method simulations, encompass all the previously mentioned grids, except for the body-fitted grids discretizing the rotor blades. The only difference between these two grid systems is in the vicinity of the zone containing the momentum source terms.

One of the grid systems, originally created with the AD method in mind, places no emphasis on creating a grid that uniformly distributes points in the circumferential direction around the rotor location, since the original assumption was that it would not have an impact in the resulting flow field, given that the source terms are distributed uniformly in this direction. Therefore, one of the grids from the SM grid system surrounding the rotor geometry was re-purposed as an actuator region zone where the source terms are active in the AD method. One of the interesting features of this grid block is the fact that its axial extent varies in the radial direction according to the local blade chord, as it varies along the blade span. Secondly, its grid lines are oriented to take into account the blade twist, which was found necessary to properly capture the blade wakes during preliminary simulations in the sliding mesh case using URANS. These features of the actuator region grid block are illustrated in Figure 17(a). Accordingly, this grid system is labeled Actuator Region non-Uniform (AR-nU).

A second grid system, created with the AL method in mind, tries to amend this by having a re-designed set of grids around the rotor region with uniformly distributed grid points in the circumferential direction. Additionally, the axial extent of the actuator region zone for this grid system is constant throughout the radial

Grid Name	# Grid Points	# Solution Points	Used in		
			Sliding Mesh	Actuator Disk	Actuator Line
SM	213 278 839	172 623 441	✗		
AR-nU	174 714 879	147 824 517		✗	✗
AR-U	174 714 879	147 842 629			✗

Table 3: Summary of grid information for the three grid systems developed for the SDT case.

coordinate. Correspondingly, this grid system is labeled Actuator Region Uniform (AR-U). The uniformity of this grid block is evident in Figure 17(b). Note that the number of grid points was kept constant for both the AR-nU and AR-U grid systems. Sensitivity of the AL method to these actuator region grid features will be assessed. Table 3 summarizes grid information and usage over the three methods considered in the present work.

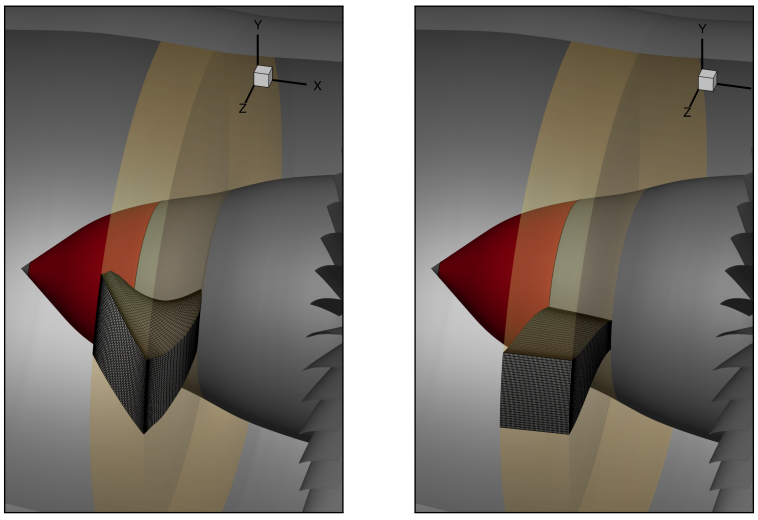

(a) Grid slice of the non-uniform actuator region zone in the AR-nU grid system.

(b) Grid slice highlighting the uniform nature of the actuator region zone in the AR-U grid system.

Figure 17: Comparison between the actuator region grid zones in the AR-nU and AR-U grid systems.

Slices of the near-body grid systems for each computational setup are presented in Figure 18. Most of the internal flow grids consist of structured point-matched multi-block grids, with the exception of the rotor and OGV stages, which are overset with the inflow grid blocks, the interstage region, and the outflow blocks downstream of the OGVs. A small cap grid removes the spinner nose singularity, and it is overset with the two incoming upstream grid blocks which cover the nacelle inlet region into the far-field. The body-fitted grids in the outer nacelle region are grown to a distance of about one nacelle radius (roughly 11 in), and are then overset with an inner Cartesian block composed of nearly isotropic cells in the vicinity of the fan rig. This block creates a smooth transition between the near-body grids and the outer Cartesian off-body mesh that stretches more aggressively to the far-field boundaries.

A brief description of the computational setup for each method applied to the SDT test case will now be provided. The actuator disk zone shown in yellow in Figure 18(a) was easily setup by revolving a two-dimensional grid that encompasses the blade geometry. Since a steady RANS approach is used in this method, a rotating wall boundary condition is enforced in the spinner (shown in red) to match the blade rotational velocity of 7808 RPM.

The AL method, when used in conjunction with the sliding mesh algorithm, allows for a reduction in computational cost when compared to an isolated AL methodology. By avoiding the execution of a point-locating algorithm at each timestep (for every point in the actuator line point cloud) due to the relative motion of the actuator line points relative to the background grid system, one can instead perform this computation once as a pre-processing step, provided the relative motion is removed by making use of the sliding mesh algorithm to rotate the background grids. This technique was employed for the actuator line unsteady RANS simulations presented hereafter. Figure 18(b) shows a slice of the AR grid system with a representation of the blade shape colored in yellow, as provided by an iso-surface of the body force obtained using a non-isotropic Gaussian distribution for 3D control points (see Section 2). The magenta grid surrounding the actuator lines rotates to match the blade rotational velocity of 7808 RPM, taking advantage of a sliding mesh technique to lower its computational cost per timestep. Since the remaining grids are static, a rotating wall boundary condition is enforced in the spinner (shown in red), as was done in the actuator disk simulations.

The setup for the sliding mesh simulations using unsteady RANS on the SM grid system is similar. Additional zones around the rotor blades are added to the list of rotating grids, to ensure that all blade body-fitted grids are encompassed by the rotating portion of the grid system. These are shown in magenta in Figure 18(d). The surfaces colored in red now belong to zones that rotate with the blades, meaning the rotating spinner wall is automatically enforced with the default viscous wall boundary condition applied elsewhere. As for the rotating grids just downstream of the spinner, a stationary wall boundary condition is enforced.

5.3 Procedure for Blade Load Distribution Computation

Since thrust and torque values for the R4 experiment were not publicly available to the authors' knowledge, the first step was to simulate the entire rig with URANS using the sliding mesh methodology. Thrust and torque values are then estimated using the procedure described below, and are used as inputs to the AD and AL methods.

The timestep for the sliding mesh URANS case is set to $1/704^{\text{th}}$ of the total rotor revolution time, and initialization of the flow field takes place in three stages for reasons related to solver stability:

1. Firstly, the flow field is initialized using freestream conditions and run for 10 revolutions at a CFL of 10 until the startup transients developed in the flow field are convected out. A Koren limiter helps bound the convective fluxes that are computed at this stage.

2. The CFL is then ramped up to 100 for two more rotor revolutions;

3. Finally, 10 to 12 rotor revolutions are simulated, until at least 10 rotor revolutions of statistically steady state flow are captured.

The solution is then averaged using data from the last 10 rotor revolutions using a simple arithmetic average of every flow quantity over the number of timesteps considered. Results for the sliding mesh case are presented side-by-side with actuator disk and actuator line results, to facilitate drawing comparisons between flow field features of each method. These results will establish a baseline for what the actuator disk and actuator line cases could hope to achieve when compared to the experimental data. Upon obtaining the arithmetic average of the sliding mesh flow field over 10 rotor revolutions, the pressure coefficient on the surface of the rotor blades is extracted from the solution using a set of tools from the Chimera Grid Tools (CGT) software package [65], namely MIXSUR, OVERINT and TRILOAD. In this process, the solution is interpolated to a set of zipper grids defining the rotor blade surfaces after removal of the overlapping grids present in the original overset grid system (MIXSUR). This step is followed by integration of the surface loads over the entire surface using OVERINT. This procedure was utilized to obtain the total thrust and torque values to apply in the AD and AL methods (4041.1156 N and -904.5109 N m, respectively).

A similar process was used to extract the load distribution along the blade span. Applying the steps just described with MIXSUR and OVERINT, the surface of a single rotor blade was then sliced into several equally-spaced bins along the radial axis using TRILOAD, as illustrated in Figure 19(a). A total of 1000 bins were used to properly capture the load distribution as it tends to zero near the blade root and tip regions. The pressure coefficient is integrated over the surface of each bin, resulting in a load distribution that can

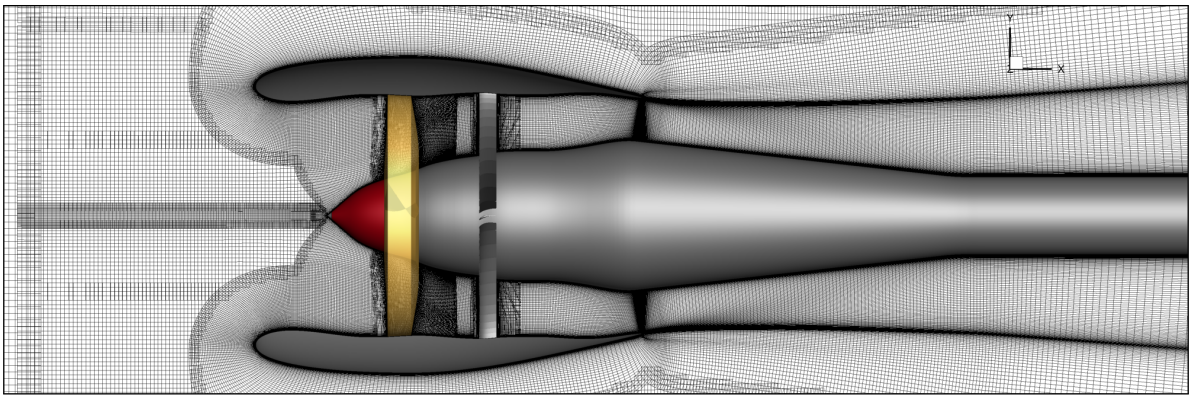

(a) Slice of the AR-nU grid at Z = 0 m with actuator disk zone highlighted in yellow.

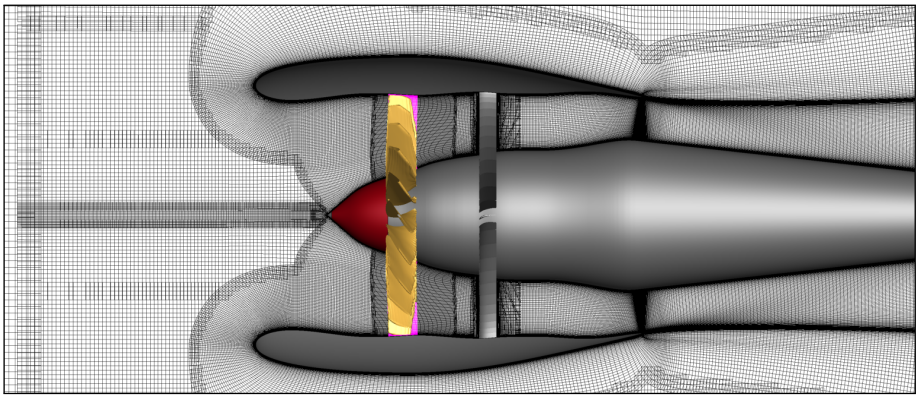

(b) Slice of the AR-U grid at Z = 0 m with yellow isocontour highlighting the actuator line shape. The zone highlighted in magenta rotates with the actuator lines using a sliding mesh technique.

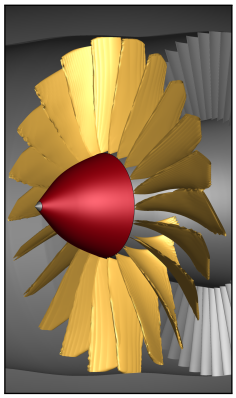

(c) Zoomed-in view of actuator lines isocontour.

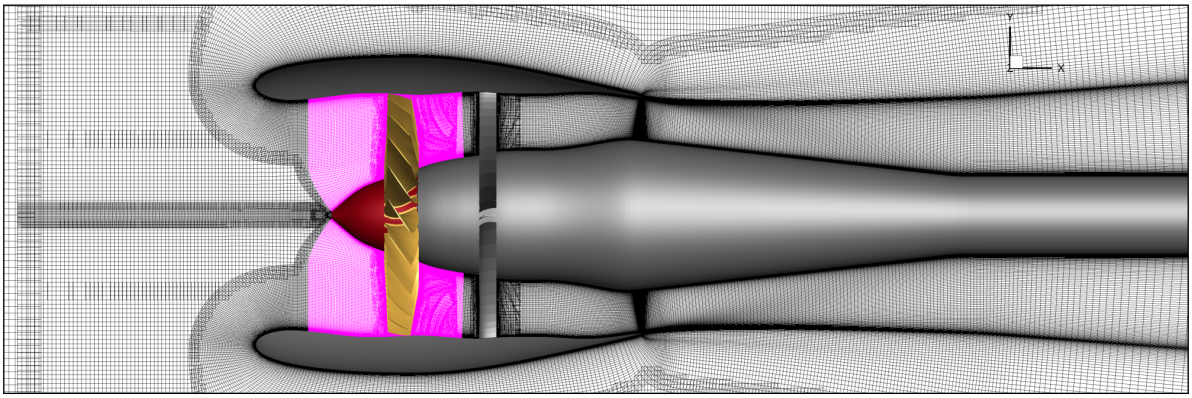

(d) Slice of the SM grid at Z = 0 m with sliding mesh zones highlighted in magenta.

Figure 18: Grid slices highlighting the difference in setup for each computational methodology considered. A rotating wall boundary condition enforcing a rotational velocity of 7808 RPM is applied to the spinner surface, shown in red, whenever the grid zones it belongs to are stationary.

be used in the AD and AL methods to more accurately weigh the source terms radially. Two of the load distributions resulting from this step, namely the axial force coefficient $C_{F,x}$ and moment coefficient around the blade rotational axis $C_{m,x}$, are presented in Figures 19(b) and 19(c). These load profiles, normalized such that the total area under each curve equals 1, are used to distribute the total thrust and torque values along the radial direction, respectively. The constant loading case, as well as the Goldstein optimum load

distribution [66] are also plotted in the same figures.

A limitation of the procedure described above using TRILOAD results from the fact that the blade slices are taken perpendicular to a given Cartesian axis. As shown in Figure 19(a), the cuts taken close to the blade root result in slices that are open in the region where the blade meets the hub. This is a by-product of the growing-radius profile exhibited by the hub at this location, and leads to an nonphysical load distribution in the first 10 % of the root-to-tip distance, as evident on the black profile shown in Figure 19(b). The team plans on removing this limitation in future work requiring this load distribution computation, but for the meantime a temporary workaround utilized in the present work was to take the thrust value of the first blade slice that does not intersect the hub, and linearly interpolate its value down to the physically sound value of zero at the blade root. The load distribution resulting from this approximation is shown in red in Figure 19(b) (curve tagged with *wHC*, meaning *with hub correction*). The reason for the apparent decrease in thrust towards the tip compared to the black curve stems from the normalization procedure performed on the curves shown (maintaining the area under each curve equal to 1), and should be interpreted while keeping in mind that the total thrust and torque values applied for each distribution does not change. Finally, no corrections were performed on the moment coefficient, and both cases (*with/without hub correction*) share the same profile. Comparisons between the different loading distributions will be presented in Section 5.4.

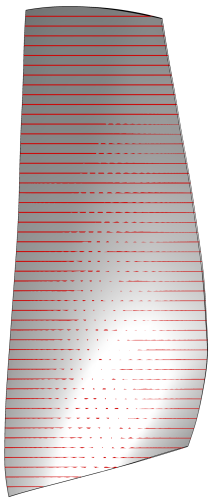

(a) Rotor blade cuts for load computations. Only 51 bins are shown, out of the 1000 bins used for the final load profile computation.

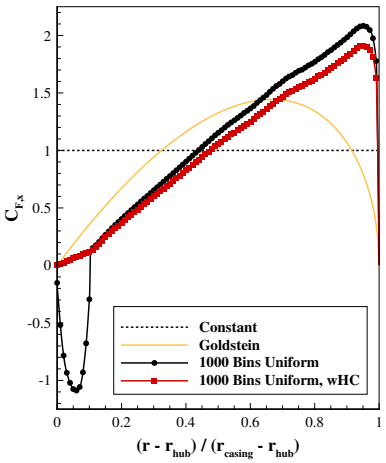

(b) Axial force coefficient profiles obtained with TRILOAD as a function the radial coordinate along the blade span. The tag *wHC* means *with hub correction*.

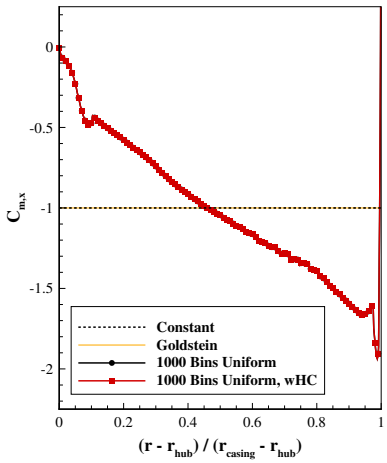

(c) Moment coefficient profiles around the rotational axis of the blade, obtained with TRILOAD, as a function the radial coordinate along the blade span. No hub corrections were performed for the moment coefficient, and both profiles are identical.

Figure 19: Single-blade axial force and moment coefficients as a function of the radial coordinate along the blade span obtained from the sliding mesh mean flow solution using TRILOAD. Goldstein [66] and constant loading profiles also shown for reference.

5.4 Results

In this section, results for the three computational methodologies described above will be presented. Several simulation setups were tested for the actuator disk and actuator line methods, in an attempt to match the results obtained with the sliding mesh technique. This will be a first step in establishing best practices for the group when running simulations with the lower fidelity models.

The following summarizes the different simulations performed on the AD/AL methods:

- Blade loading variations - custom load distribution computed using TRILOAD, both *with* and *without* the *hub corrections* (*wHC* and *woHC*, respectively) , as discussed in the context of Figure 19. A constant and Goldstein load distributions were also tested.

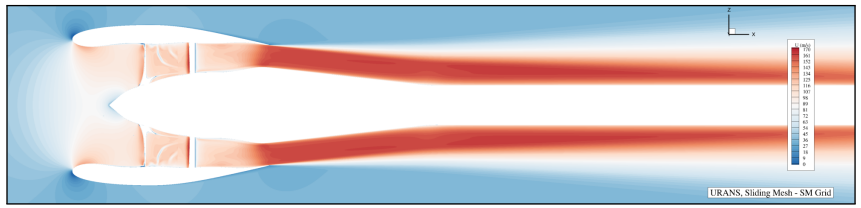

(a) Sliding mesh, SM grid.

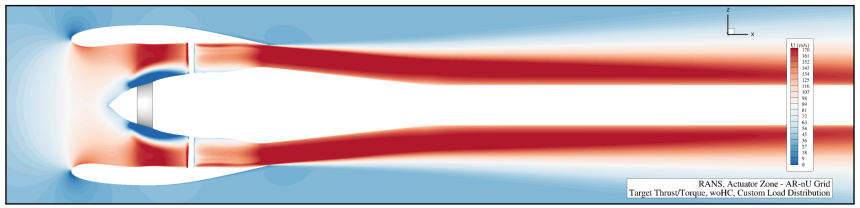

(b) Actuator disk, custom loading *woHC*, *TTT*, AR-nU grid.

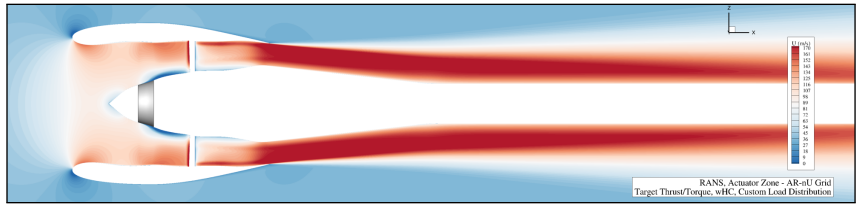

(c) Actuator disk, custom loading *wHC*, *TTT*, AR-nU grid.

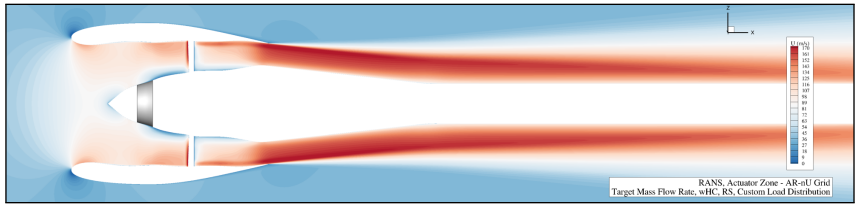

(d) Actuator disk, custom loading *wHC*, *Tmdot*, *RS*, AR-nU grid.

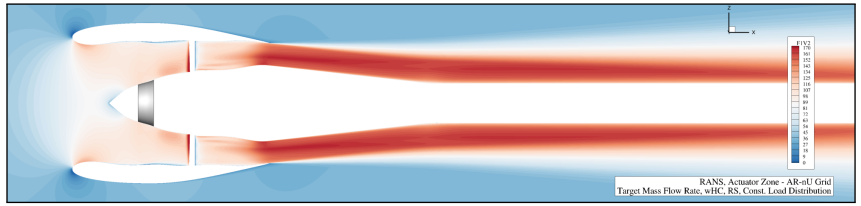

(e) Actuator disk, constant loading, *Tmdot*, *RS*, AR-nU grid.

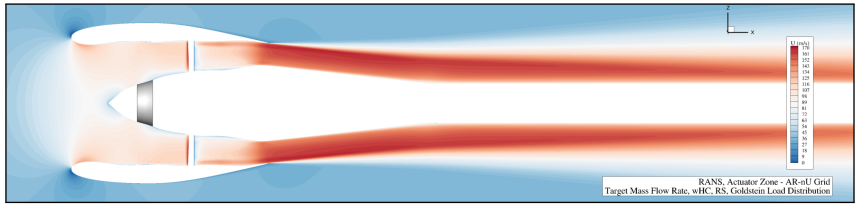

(f) Actuator disk, Goldstein loading, *Tmdot*, *RS*, AR-nU grid.

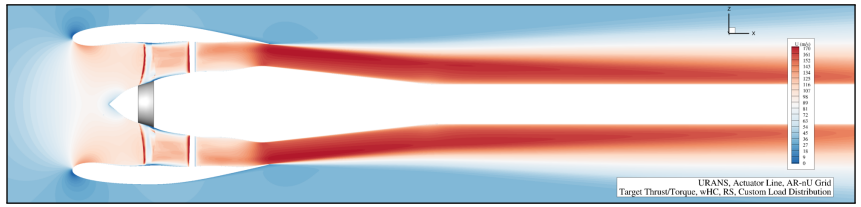

(g) Actuator line, custom loading *wHC*, *TTT*, *RS*, AR-nU grid.

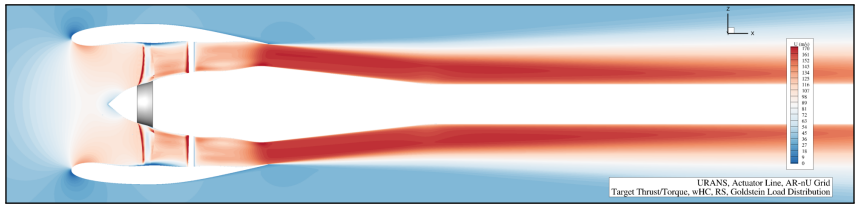

(h) Actuator line, Goldstein loading, *TTT*, *RS*, AR-nU grid.

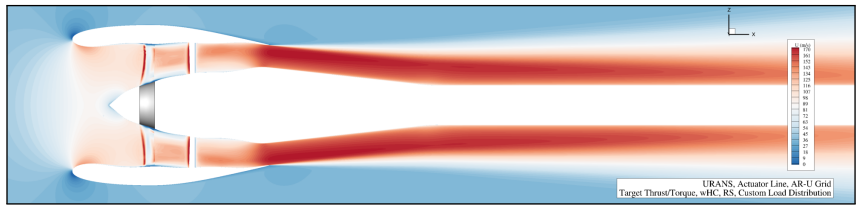

(i) Actuator line, custom loading *wHC*, *TTT*, *RS*, AR-U grid.

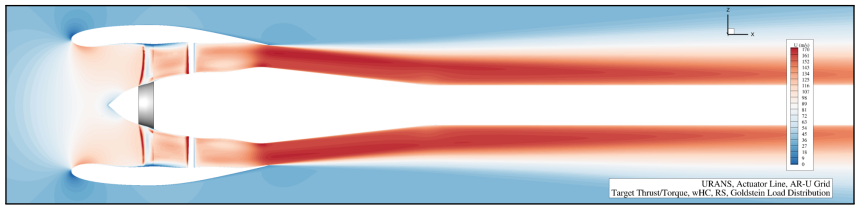

(j) Actuator line, Goldstein loading, *TTT*, *RS*, AR-U grid.

Figure 20: Comparison of axial velocity plots cutting through the engine across several simulated cases spanning the three computational methods employed in the present work - sliding mesh (URANS), actuator disk (RANS) and actuator line (URANS).

	Experimental Data	Sliding Mesh	Actuator Disk					Actuator Line			
Relative Computational Cost											
	-	1.0	0.02					0.68			
Fig. 20	-	(a)	(b)	(c)	(d)	(e)	(f)	(g)	(h)	(i)	(j)
Grid	-	SM	AR-nU					AR-nU		AR-U	
Load Profile	-	-	Custom, *woHC*	Custom, *wHC*		Constant	Goldstein	Custom, *wHC*	Goldstein	Custom, *wHC*	Goldstein
Setup	-	-	*TTT*	*TTT*	*Tmdot, RS*	*Tmdot, RS*	*Tmdot, RS*	*TTT, RS*		*TTT, RS*	
$\dot{m}$ (kg/s)	26.535	26.675	29.979	29.593	26.675	26.427	26.685	27.577	27.383	27.483	27.288
P_0 Ratio	1.159	1.159	1.210	1.204	1.164	1.156	1.160	1.174	1.171	1.175	1.700
T_0 Ratio	1.049	1.050	1.073	1.059	1.047	1.046	1.046	1.066	1.065	1.066	1.065
Percent Relative Error											
$\dot{m}$	-	0.53*	12.39	10.94	0.00	-0.93	0.04	3.38	2.65	3.03	2.30
P_0 Ratio	-	0.02*	4.41	3.88	0.44	-0.31	0.08	1.31	0.99	1.32	0.92
T_0 Ratio	-	0.11*	2.19	0.84	-0.26	-0.38	-0.38	1.46	1.42	1.51	1.37

Table 4: Summary of performance metrics results obtained for all SDT cases simulated, with an estimate of the relative computational cost for each method taking the sliding mesh as a baseline. Results are presented for several variations of blade loading - custom load profile, *with* (*wHC*) and *without* (*woHC*) *hub corrections*, Goldstein and constant load profiles - and setup - *targeting* the *thrust/torque* (*TTT*) or the *mass flow rate* (*Tmdot*) of the sliding mesh case. Sensitivity to modeling the *rotating spinner* (*RS*) using a rotating wall boundary condition was also assessed. Total pressure and temperature ratios are taken relative to their static freestream values. Percent error taken relative to the sliding mesh results. *For the sliding mesh results, percentage error is reported relative to the experimental data.

- Thrust value applied - two variants were tested, one that *targets* the *thrust/torque* values obtained from running TRILOAD on the sliding mesh case, and another that directly *targets* the *mass flow rate* (*TTT* and *Tmdot*, respectively).
- Modeling of the spinner wall rotation (*rotating spinner*, or *RS*) using a viscous rotating wall BC.
- Shape of the actuator disk/actuator line region, following the discussion in Section 5.2 - *non-uniform* versus *uniform* grid (AR-nU and AR-U grids, respectively).

A summary of the results obtained for the SDT case is compiled in Table 4. Results presented therein will be referenced throughout the discussion that follows. Figure 20 contains an overview of the sensitivity observed in axial velocity across several simulations performed. Starting with the sliding mesh case shown in Figure 20(a), the first test performed with the AD method was to take the thrust/torque values obtained from TRILOAD, as well as the custom load distributions shown in black in Figures 19(b) and 19(c), and run a case on the AR-nU grid. The resulting flow field is presented in Figure 20(b). A large separation region is observed near the hub where the actuator region is active, caused by the non-physical negative thrust characterizing the thrust profile directly obtained from TRILOAD. Applying the hub correction (Figure 20(c)) improves the hub flow field, but still results in too high a mass flow rate through the stage, by about 11 % compared to the sliding mesh case, as reported in Table 4.

This result led the team to attempt targeting the mass flow rate by lowering the thrust value applied in the actuator disk region. These simulations, labeled *Tmdot* and presented in Figures 20(d) through 20(f), have a total applied thrust value of about 79 % of the original thrust reported by TRILOAD. Referring to Table 4 once again, a significant improvement in the total pressure and temperature performance metrics through the stage is observed for these cases. Looking at Figure 20(d), however, it is observed that the low velocity region just downstream of the actuator disk near the hub is still present. The constant loading case (Figure 20(e)) improves in this regard, but introduces a similar effect near the rotor tip. Finally, the Goldstein load distribution case (Figure 20(f)) appears to improve the near-hub flow field without affecting the casing boundary layer downstream of the rotor tip significantly.

Taking a closer look at the mean flow velocities at the hot-wire probe station 1, downstream of the rotor, gives additional insight to the differences between the actuator disk and sliding mesh cases (Figures 21(c)

through 21(e)). Here, the low near-hub velocity of the custom load profile is evident (magenta curve), as is the near-tip low velocity region of the constant load profile case (green curve). The Goldstein load profile (orange curve) shows good agreement in the axial velocity at the outer half of the internal flow path, but still underpredicts the axial velocity towards the hub. Surprisingly, the constant load profile has a better agreement with the experimental data than the sliding mesh case when it comes to the radial velocity, which has been identified as a common discrepancy among other groups [63]. In general, however, the actuator disk results tend to underpredict the radial velocity component closer to the hub, while overpredicting it near the casing. More interesting is the fact that none of the actuator disk cases targeting mass flow rate come close to predicting the same tangential velocity component. This quantity is significantly underpredicted in magnitude when compared to both the experimental data and the sliding mesh results.

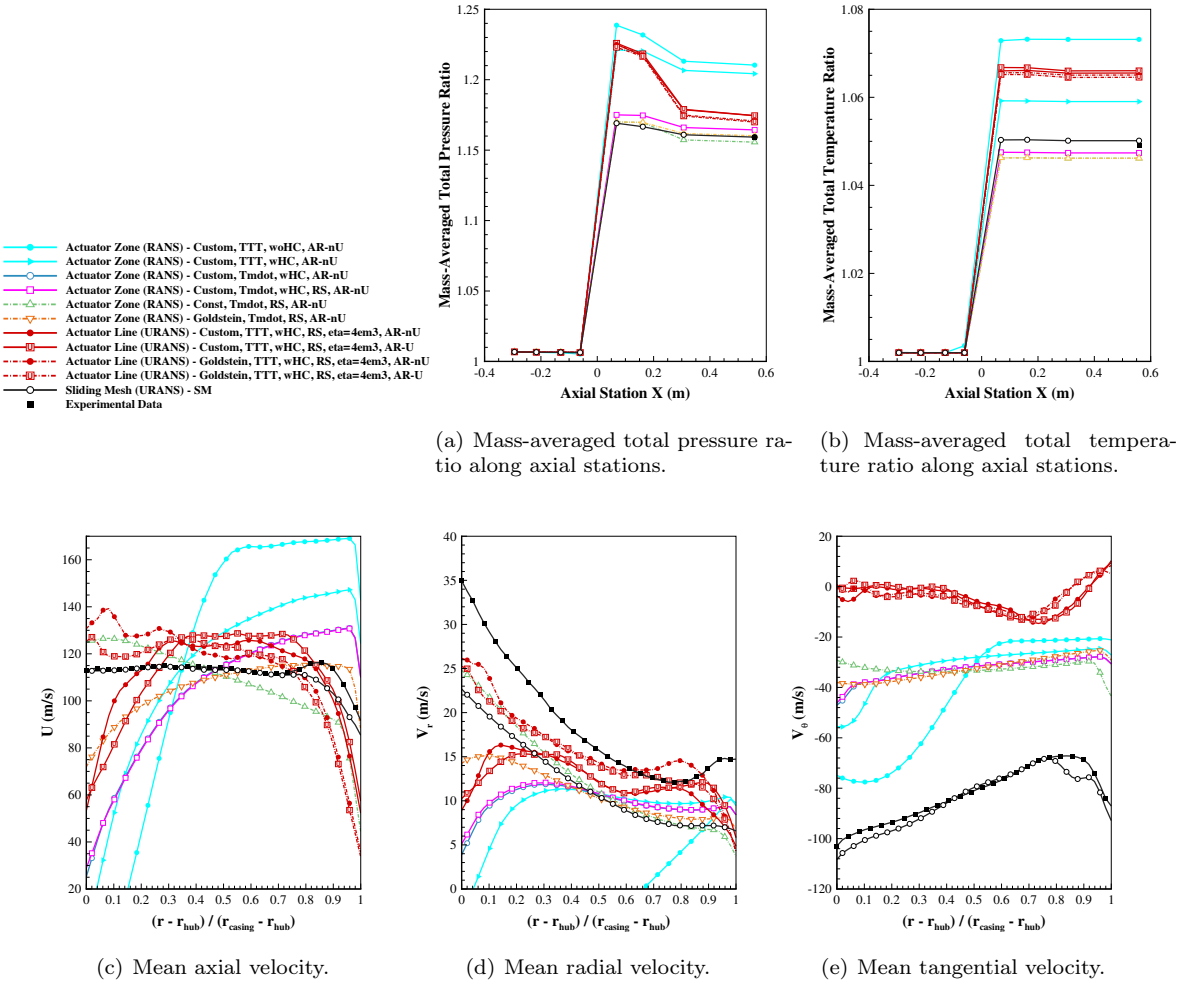

(a) Mass-averaged total pressure ratio along axial stations.

(b) Mass-averaged total temperature ratio along axial stations.

(c) Mean axial velocity.

(d) Mean radial velocity.

(e) Mean tangential velocity.

Figure 21: Comparison of stage performance metrics and mean velocity profile data measured at hot-wire probe station 1 between the different methods and the experimental data.

One possible explanation for this behavior, and also for the fact that none of the slices shown in Figure 20 match the sliding mesh results in a convincing manner, is the fact that the current implementation of the actuator disk model in the code only considers the axial ($C_{F,x}$) and tangential ($C_{F,\theta}$, resulting in $C_{m,x}$) components of force that the blade exerts in the flow field. However, turbomachinery blades commonly twist in a complex manner, potentially adding radial force contributions that are not taken into account. This is also true for the actuator line implementation as it stands. Therefore, allowing for the source term force vector to exhibit a radial component that may vary along the span (as the thrust and torque distributions

already do) has been identified as a potential target for future work to improve accuracy with these lower fidelity methods. Finally, it should be mentioned that other cases with a different BC for the actuator disk hub wall (shown in grey in Figures 20(b) through 20(j)) were simulated, but its effects are not presented here. Namely, a rotating viscous wall BC in the spinner (cases labeled with *RS*) resulted in slightly different radial and tangential velocity components closer to the hub (blue curves in Figures 21(d) and 21(e)). A slip wall BC was also tested, with very little effect on the resulting mean flow.

Returning to Figure 20, we now turn our attention to the actuator line results (Figures 20(g) through 20(j)). Four cases are presented, two of which were simulated on the AR-nU grid and the other two on the AR-U grid, and both the custom and Goldstein load distributions were simulated. Overall, the slices of axial velocity component still exhibit the same shortcomings of the actuator disk simulations. The custom loading case presents a low-speed region downstream of both the actuator line hub and tip regions, while the Goldstein load profile shows an improvement near the hub, but a larger low-speed flow pocket near the tip. These observations are also valid for the simulations performed on the AR-U grid, meaning that using the uniform grid did not improve these particular flow field features. One of the main conclusions from these observations is that the flow field downstream of the actuator line presents a large sensitivity to the type of blade loading used. This makes the increased accuracy that a blade loading force vector pointing in a general direction would provide an even more desirable feature to build in the future.

Zooming in to the mean flow velocity profiles in Figures 21(c) through 21(e), the difference between the two loading distributions is now easily seen near the hub. The custom load profile curves show a lower axial velocity component near the hub, whereas the Goldstein load distribution is able to carry the internal flow velocity closer to the wall. However, both load distributions suffer from an excessively large boundary layer near the casing. The Goldstein load distribution again outperforms the custom one when it comes to the radial velocity component, but both perform poorly when it comes to the tangential velocity component. Whatever tangential momentum source terms are added inside the actuator line region, the tangential velocity field they induce diffuses too quickly and does not carry downstream to the measurement station upstream of the OGVs, resulting in near-zero tangential velocities. In this regard, the AL method appears to be outperformed by the actuator disk.

Performance metrics along the fan stage were also compiled for all cases considered, and are plotted in Figures 21(a) and 21(b). These show that, when targeting the correct mass flow rate through the fan stage, the AD method outperforms the AL method across the stage. In particular, the AL method tends to overpredict the total pressure just downstream of the actuator line region, and the total temperature over the whole range. Total pressure predictions using the Goldstein loading profile provide the closest agreement with the sliding mesh case. Total temperature, on the other hand, is slightly underpredicted in this case, and is better captured with the custom blade loading profile after hub corrections are introduced.

A final compilation of results allowing for a convenient qualitative comparison between actuator disk, actuator line and sliding mesh flow field features is presented in Figure 22. The actuator region cases selected for these plots were:

- Actuator disk - custom load distribution, *wHC*, *Tmdot*, *RS*, AR-nU grid.
- Actuator line - custom load distribution, *wHC*, *TTT*, *RS*, AR-U grid.

Each slice shows the average flow field - axial, radial and tangential velocity components, pressure and temperature - at a given axial station, ranging from the hot wire measurement station 1 to the nozzle exit, for each simulation methodology considered in this work. The top row, showing results at the hot wire probe station 1, presents the most variability across all methods. As we move downstream of the OGV, certain similarities in the begin emerging, given that the OGVs now play the dominating geometric role. This resemblance, however, only carries to the nozzle exit for the actuator disk results. The actuator line results lack the structure of the sliding mesh and actuator disk results, likely due to the fact that the OGVs are unable to remove the tangential velocity component to the extent observed in the latter methods. This is easily seen in Figure 22(h), where the actuator line results show a prevalent positive tangential velocity in the inner flow field region, whereas the actuator disk and sliding mesh results are mostly swirl-free. As for the actuator disk results, the bottom row of results is very revealing. The axial velocity plot (Figure 22(k)) shows a thick low velocity region close to the hub and a high velocity region closer to the casing, relative to the sliding mesh case. This supports the claim that, even though the mass flow rate for the two

cases is the same, that simply results from a balance between overpredicted and underpredicted values. For situations where knowledge of the actual flow field is important, this shows that there is still significant room for improvement in the current implementation of both AD and AL methods for internal flow applications. On the other hand, when performance metrics are the quantities of interest, the AD method appears to predict them reasonably well, at two orders of magnitude lower computational cost. It is in the former range of situations where the actuator line method can find its niche application, since it provides a considerable cost savings when compared to the sliding mesh case, both computationally (refer to Table 4) and in the grid generation stage.

6 Conclusion

In this study, three propulsion models with increasing fidelity were implemented in the Launch Ascent and Vehicle Aerodynamics Solver (LAVA) framework and applied to a suite of test-cases. These models are actuator disk method, actuator line method and sliding disk method. Several different test-cases have been chosen in an attempt to address all applications that are relevant for the research interests utilizing the LAVA solver framework. This included applications with tip-mounted and top-mounted rotors as well as turbofans. For the actuator disk and line methods a source term is applied to the momentum and energy equations with various load distributions. The correct implementation of the source-term-based approach was validated by comparing it with an analytical solution derived from 1D momentum theory for an isolated rotor in hover. Simulations for the top-mounted GIT configuration were performed and compared with data from experiments as well as RANS from literature. As the rotor and fuselage shaft were not considered in this study, a deviation from experiments can be seen in the surface pressure distribution. Nevertheless, an overall good agreement has been observed with these simplified methods especially comparing with simulations reported in the literature. A strong effect of the selected load distribution on velocity profiles and surface pressures has been demonstrated making it crucial to choose an appropriate loading for the given application. For the GIT configuration it has been shown that choosing a linear disk loading produces closer values to the experiment. A good agreement for the tip-mounted experiment performed by Samuelsson was observed with the actuator disk. The effect of the rotor swirl on the wings was captured well both qualitatively as well as quantitatively. This simple validation study showed that actuator disk methods are a good choice to model effects of rotors on vehicles without the need for computationally expensive time-resolved simulations.

In a second step the carefully validated methods were utilized for engineering applications within NASA's ARMD projects. First the generation of a database for the Maxwell X-57 aircraft was described which showed the effect of rotors on the overall lift and drag curve of the configuration. It has been demonstrated that it is crucial to include the effects induced by the tip mounted rotors in the analysis. However given the amount of simulations necessary to generate this database, performing time-resolved unsteady RANS simulations including the actual blades would not have been feasible. This makes the simple actuator disk method a highly valuable tool for aerodynamic predictions due to it's reduced costs.

A more detailed comparison between the three propulsion methods was performed for the final application case where both RANS as well as uRANS simulations were conducted on NASA's R4 STD configuration. First simulations were performed using a sliding mesh methodology in which the blades were fully meshed. From this initial simulation a load distribution as well as thrust and torque values were derived utilizing a set of tools taken from the Chimera Grid Tools (CGT) software package. Utilizing the obtained values several steady RANS simulations using the actuator disk model were performed comparing a constant loaded disk, a Goldstein optimum loaded disk as well as a custom loaded disk. A higher mass flow rate compared to the sliding disk method was observed for the custom profile. Both the custom profile as well as the constant profile show a pattern of flow separation near the hub and tip respectively. The Goldstein profile seems to agree the best with the sliding mesh. Significant improvements were found by applying a mass-flow rate matching procedure which was achieved by reducing the supplied thrust value.

Finally both the sliding mesh as well as actuator disk methods were compared with the actuator line method. A major benefit of the actuator line method is that no explicit knowledge of the blade shape is necessary. This is particular of interest as blades in propulsion applications are often proprietary and not readily available. In addition, the computational costs of the actuator line method were about 60% lower compared to the sliding disk approach. The steady state actuator disk method resulted in a reduction of

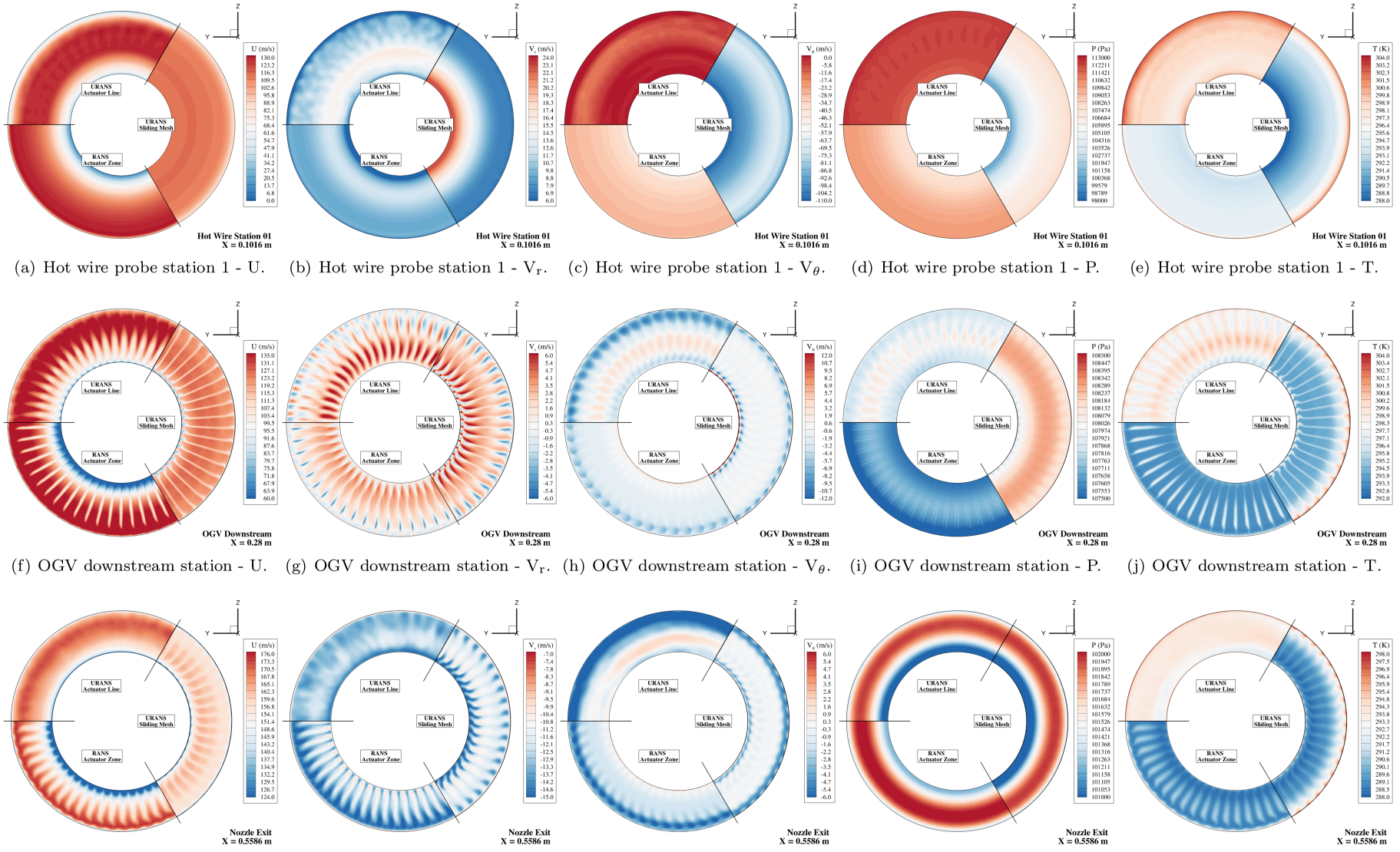

(a) Hot wire probe station 1 - U. (b) Hot wire probe station 1 - V_r. (c) Hot wire probe station 1 - V_θ. (d) Hot wire probe station 1 - P. (e) Hot wire probe station 1 - T.

(f) OGV downstream station - U. (g) OGV downstream station - V_r. (h) OGV downstream station - V_θ. (i) OGV downstream station - P. (j) OGV downstream station - T.

(k) Nozzle exit station - U. (l) Nozzle exit station - V_r. (m) Nozzle exit station - V_θ. (n) Nozzle exit station - P. (o) Nozzle exit station - T.

Figure 22: Comparison of mean flow contours for the five primitive variables at three distinct axial stations, for the three computational methodologies employed - sliding mesh case (SM grid), actuator disk case (AR-nU grid, custom loading profile with hub corrections, targeting mass flow rate of sliding mesh case) and actuator line case (AR-U grid, custom loading profile with hub corrections, targeting thrust/torque values obtained from sliding mesh case).

costs of two orders of magnitude. This reduction is mainly based on the savings in grid points by not having the model the blade geometry. In addition the manual mesh generation effort is reduced due to the absence of the blade geometry. When comparing velocity profiles with hot-wire measurements bigger differences can be observed for the actuator disk method as well as the actuator line method. A good agreement was achieved with the sliding mesh method. This is likely due to the fact that the current implementation of the actuator disk and line method only consider forces in the tangential and axial direction. However, turbomachinery blades commonly twist in a very complex manner, potentially adding force contributions in radial directions. The effect of a more complex force distribution will be discussed in future work.

Acknowledgments

This research is supported in part by the Advanced Air Transport Technology (AATT) project under NASA's ARMD Advanced Air Vehicles Program (AAVP). Computer time was provided by the NASA Advanced Supercomputing (NAS) facility at NASA Ames Research Center. The authors would like to thank Jonathan Chiew from NASA Ames Research Center for helpful advice and feedback. We would also like to thank our LAVA team members Leonardo Machado for time spent testing the actuator disk implementation within their project related work for NASA.

References

[1] C. Kiris, J. Housman, M. Barad, C. Brehm, E. Sozer, and S. Moini-Yekta. Computational Framework for Launch, Ascent, and Vehicle Aerodynamics (LAVA). *Aerospace Science and Technology*, 55:189–219, August 2016.

[2] X-57 maxwell.

[3] Thomas Edwards and George Price. evtol passenger acceptance. Technical report, 2020.

[4] Alex M Stoll, Edward V Stilson, JoeBen Bevirt, and Percy P Pei. Conceptual design of the joby s2 electric vtol pav. In *14th AIAA Aviation Technology, Integration, and Operations Conference*, page 2407, 2014.

[5] Kyle A Pascioni, Michael E Watts, Mary Houston, Andrew Lind, James H Stephenson, and Jeremy Bain. Acoustic flight test of the joby aviation advanced air mobility prototype vehicle. In *28th AIAA/CEAS Aeroacoustics 2022 Conference*, page 3036, 2022.

[6] RM Ardito Marretta, G Davi, G Lombardi, and A Milazzo. Hybrid numerical technique for evaluating wing aerodynamic loading with propeller interference. *Computers & fluids*, 28(8):923–950, 1999.

[7] Jinsoo Cho and Jaeheon Cho. Quasi-steady aerodynamic analysis of propeller–wing interaction. *International journal for numerical methods in fluids*, 30(8):1027–1042, 1999.

[8] B Chandrasekaran. *Methods for the Prediction of the Installation Aerodynamics of a Propfan at Subsonic Speeds*, volume 3887. National Aeronautics and Space Administration, Scientific and Technical Ŏ026, 1985.

[9] Per Lotstedt. Accuracy of a propeller model in inviscid flow. *Journal of Aircraft*, 32(6):1312–1321, 1995.

[10] Alasdair Thom and Karthikeyan Duraisamy. Computational investigation of unsteadiness in propeller wake–wing interactions. *Journal of Aircraft*, 50(3):985–988, 2013.

[11] Matthew J Churchfield, Scott J Schreck, Luis A Martinez, Charles Meneveau, and Philippe R Spalart. An advanced actuator line method for wind energy applications and beyond. In *35th Wind Energy Symposium*, page 1998, 2017.

[12] AG Brand, NM Komerath, and HM McMahon. Wind tunnel data from a rotor wake/airframe interaction study. Technical report, Georgia Institute of Technology, 1986.

[13] Ingemar Samuelsson. Low speed wind tunnel investigation of propeller slipstream aerodynamic effects on different nacelle/wing combinations. In *ICAS, Congress, 16 th, Jerusalem, Israel*, pages 1749–1765, 1988.

[14] Goktan Guzel and Özgür Atesoglu. Implementation and validation of an actuator disk model for aerodynamic analysis of propelled uavs. In *AIAA Atmospheric Flight Mechanics Conference*, page 2669, 2014.

[15] C. Hughes. Aerodynamic performance of scale-model turbofan outlet guide vanes designed for low noise. In *40th AIAA Aerospace Sciences Meeting & Exhibit*, 2002.

[16] Edmane Envia. Fan noise source diagnostics test - vane unsteady pressure results. In *8th AIAA/CEAS Aeroacoustics Conference & Exhibit*, 2002.

[17] Laurence Heidelberg. Fan noise source diagnostic test - tone modal structure results. In *8th AIAA/CEAS Aeroacoustics Conference & Exhibit*, 2002.

[18] Aditya S Ghate, Gaetan K Kenway, Gerrit-Daniel Stich, Oliver M Browne, Jeffrey A Housman, and Cetin C Kiris. Transonic lift and drag predictions using wall-modelled large eddy simulations. In *AIAA Scitech 2021 Forum*, page 1439, 2021.

[19] Aditya S Ghate, Jeffrey A Housman, Gerrit-Daniel Stich, Gaetan Kenway, and Cetin C Kiris. Scale resolving simulations of the nasa juncture flow model using the lava solver. In *AIAA Aviation 2020 Forum*, page 2735, 2020.

[20] James C Jensen, Gerrit-Daniel Stich, Jeffrey A Housman, Marie Denison, and Cetin C Kiris. Lava simulations for the 3rd aiaa cfd high lift prediction workshop using body fitted grids. In *2018 AIAA Aerospace Sciences Meeting*, page 2056, 2018.

[21] Aditya S Ghate, Gerrit-Daniel Stich, Gaetan K Kenway, Jeffrey A Housman, and Cetin C Kiris. A wall-modeled les perspective for the high lift common research model using lava. In *AIAA AVIATION 2022 Forum*, page 3434, 2022.

[22] Cetin C Kiris, Aditya S Ghate, Jared C Duensing, Oliver M Browne, Jeffrey A Housman, Gerrit-Daniel Stich, Gaetan Kenway, Luis S Fernandes, and Leonardo M Machado. High-lift common research model: Rans, hrles, and wmles perspectives for clmax prediction using lava. In *AIAA SCITECH 2022 Forum*, page 1554, 2022.

[23] S.R. Spalart and S.A. Allmaras. A One-Equation Turbulence Model for Aerodynamic Flows. In *30th Aerospace Sciences Meeting and Exhibit, Reno, NV*, January 1992. AIAA-92-0439.

[24] Jeffrey A Housman, Cetin C Kiris, and Mohamed M Hafez. Time-derivative preconditioning methods for multicomponent flows part ii: Two-dimensional applications. *Journal of applied mechanics*, 76(3), 2009.

[25] Youcef Saad and Martin H Schultz. Gmres: A generalized minimal residual algorithm for solving nonsymmetric linear systems. *SIAM Journal on scientific and statistical computing*, 7(3):856–869, 1986.

[26] J.L. Steger and J.A. Benek. On the Use of Composite Grid Schemes in Computational Aerodynamics. Technical Memorandum 88372, NASA, 1986.

[27] W. Chan. Developments in Strategies and Software Tools for Overset Structured Grid Generation and Connectivity. In *20th AIAA Computational Fluid Dynamics Conference, Honolulu, Hawaii*, June 2011. AIAA-2011-3051.

[28] R Ganesh Rajagopalan and Jerome B Fanucci. Finite difference model for vertical axis wind turbines. *Journal of Propulsion and Power*, 1(6):432–436, 1985.

[29] F Le Chuiton. Quasi-steady simulation of a complete ec-145 helicopter: Fuselage+ main/tail actuator discs+ engines. 2005.

[30] Laith AJ Zori, Sanjay R Mathur, and RG Rajagopalan. Three-dimensional calculations of rotor-airframe interaction in forward flight. 1992.

[31] DK Hall, EM Greitzer, and CS Tan. Analysis of fan stage conceptual design attributes for boundary layer ingestion. *Journal of Turbomachinery*, 139(7), 2017.

[32] Jens Norkær Sorensen and Wen Zhong Shen. Numerical modeling of wind turbine wakes. *J. Fluids Eng.*, 124(2):393–399, 2002.

[33] Luis A Martínez-Tossas, Matthew J Churchfield, and Stefano Leonardi. Large eddy simulations of the flow past wind turbines: actuator line and disk modeling. *Wind Energy*, 18(6):1047–1060, 2015.

[34] Luis A Martínez-Tossas, Matthew J Churchfield, and Charles Meneveau. Optimal smoothing length scale for actuator line models of wind turbine blades based on gaussian body force distribution. *Wind Energy*, 20(6):1083–1096, 2017.

[35] N Troldborg, J Sørensen, and R Mikkelsen. *Actuator line modeling of wind turbine wakes Ph. D.* PhD thesis, thesis Technical University of Denmark, 2009.

[36] Pankaj K Jha, Matthew J Churchfield, Patrick J Moriarty, and Sven Schmitz. Guidelines for volume force distributions within actuator line modeling of wind turbines on large-eddy simulation-type grids. *Journal of Solar Energy Engineering*, 136(3), 2014.

[37] Man Mohan Rai. Navier-stokes simulations of rotor/stator interaction using patched and overlaid grids. *Journal of Propulsion and Power*, 3(5):387–396, 1987.

[38] Man Mohan Rai. Three-dimensional navier-stokes simulations of turbine rotor-stator interaction. part i-methodology. *Journal of Propulsion and Power*, 5(3):305–311, 1989.

[39] Gaofeng Wang, Florent Duchaine, Dimitrios Papadogiannis, Ignacio Duran, Stéphane Moreau, and Laurent YM Gicquel. An overset grid method for large eddy simulation of turbomachinery stages. *Journal of Computational Physics*, 274:333–355, 2014.

[40] Luis Ramírez, Charles Foulquié, Xesús Nogueira, Sofiane Khelladi, Jean-Camille Chassaing, and Ignasi Colominas. New high-resolution-preserving sliding mesh techniques for higher-order finite volume schemes. *Computers & Fluids*, 118:114–130, 2015.

[41] Nicolas Bettschart. Rotor fuselage interaction: Euler and navier-stokes computations with an actuator disk. In *Annual Forum Proceedings- American Helicopter Society*, volume 1, pages 419–438, 1999.

[42] David Michael O'Brien Jr. *Analysis of computational modeling techniques for complete rotorcraft configurations*. PhD thesis, Georgia Institute of Technology, 2006.

[43] Formale Angaben zum Modul and Verortung des Moduls im Studienverlauf. Fluidmechanik (t2mb9343).

[44] Alberterard Brand. An experimental investigation of the interaction between a model rotor and airframe in forward flight(ph. d. thesis). 1989.

[45] AG Brand, HM McMahon, and NM Komerath. Surface pressure measurements on a body subject to vortex wake interaction. *AIAA journal*, 27(5):569–574, 1989.

[46] S Liou, N Komerath, and H McMahon. The velocity field of a lifting rotor in low-speed forward flight. In *26th Aerospace Sciences Meeting*, page 666, 1988.

[47] David O'Brien and Marilyn Smith. Analysis of rotor-fuselage interactions using various rotor models. In *43rd AIAA Aerospace Sciences Meeting and Exhibit*, page 468, 2005.

[48] Jared C Duensing, Seung Yoo, Daniel Maldonado, Jeffrey A Housman, James C Jensen, and Cetin C Kiris. Establishing best practices for x-57 maxwell cfd database generation. In *AIAA SciTech 2019 Forum*, page 0274, 2019.

[49] Seung Yoo and Jared Duensing. Computational analysis of the external aerodynamics of the unpowered x-57 mod-iii aircraft. In *AIAA Aviation 2019 Forum*, page 3698, 2019.

[50] Alasdair D Thom. *Analysis of vortex-lifting surface interactions*. PhD thesis, University of Glasgow, 2011.

[51] Arne Stuermer. Unsteady cfd simulations of propeller installation effects. In *42nd AIAA/ASME/SAE/ASEE Joint Propulsion Conference & Exhibit*, page 4969, 2006.

[52] Asitav Mishra, Behdad Davoudi, and Karthik Duraisamy. Multiple-fidelity modeling of interactional aerodynamics. *Journal of Aircraft*, 55(5):1839–1854, 2018.

[53] Karen A Deere, Jeffrey K Viken, Sally A Viken, Melissa B Carter, Michael R Wiese, and Norma L Farr. Computational analysis of the x-57 maxwell airplane at unpowered conditions (preliminary fuselage). 2022.

[54] Mark Drela and Harold Youngren. Xrotor download page. *Massachusetts Institute of Technology,[Online]. Available: http://web. mit. edu/drela/Public/web/xrotor/*, 2014.

[55] Jared C Duensing, Jeffrey A Housman, Luis Fernandes, Leonardo Machado, and Cetin C Kiris. A reynolds-averaged navier-stokes perspective for the high lift-common research model using the lava framework. In *AIAA AVIATION 2022 Forum*, page 3742, 2022.

[56] Jared C Duensing, Jeffrey A Housman, Daniel Maldonado, James C Jensen, Cetin C Kiris, and Seung Y Yoo. Computational simulations of electric propulsion aircraft: The x-57 maxwell. In *NASA Advanced Supercomputing Advanced Modeling & Simulation (AMS) Seminar Series*, number ARC-E-DAA-TN69863, 2019.

[57] William Chan, Reynaldo Gomez, Stuart Rogers, and Pieter Buning. Best practices in overset grid generation. In *32nd AIAA Fluid Dynamics Conference and Exhibit*, page 3191, 2002.

[58] G. Podboy, M. Krupar, S. Helland, and C. Hughes. Steady and unsteady flow field measurements within a nasa 22 inch fan model. In *40th AIAA Aerospace Sciences Meeting & Exhibit*, 2002.

[59] E Envia and J Coupland. Fan broadband noise prediction workshop. In *Proceedings of the 21th AIAA/CEAS Aeroacoustics Conference*, 2015.

[60] Michael Shur, Michael Strelets, Andrey Travin, Philippe Spalart, and Takao Suzuki. Unsteady simulations of a fan/outlet-guide-vane system: Aerodynamics and turbulence. *AIAA Journal*, 56(6):2283–2297,

2018.

[61] Takao Suzuki, Philippe R. Spalart, Michael L. Shur, Michael Kh. Strelets, and Andrey K. Travin. Unsteady simulations of a fan/outlet-guide-vane system: Tone–noise computation. *AIAA Journal*, 56(9):3558–3569, 2018.

[62] Takao Suzuki, Philippe R. Spalart, Michael L. Shur, Michael K. Strelets, and Andrey K. Travin. Unsteady simulations of a fan/outlet-guide-vane system: Broadband-noise computation. *AIAA Journal*, 57(12):5168–5181, 2019.

[63] D. Casalino, A. Hazir, and A. Mann. Turbofan broadband noise prediction using the lattice boltzmann method. *AIAA Journal*, 56(2):609–628, 2018.

[64] H. Dogus Akaydin and Shishir A. Pandya. Implementation of a body force model in overflow for propulsor simulations. *35th AIAA Applied Aerodynamics Conference*.

[65] William M. Chan, Shishir A. Pandya, Stuart E. Rogers, James C. Jensen, Henry C. Lee, David L. Kao, Pieter G. Buning, Robert L. Meakin, David A. Boger, and Steven M. Nash. Chimera grid tools user's manual, version 2.2, 2018.

[66] Sydney Goldstein and Ludwig Prandtl. On the vortex theory of screw propellers. *Proceedings of the Royal Society of London. Series A, Containing Papers of a Mathematical and Physical Character*, 123(792):440–465, 1929.